

# **IMPROVED DYNAMICS MODELING OF PROXIMITY FLIGHT USING RELATIVE ORBIT ELEMENTS**

**Simone D'Amico, et al.**

**Leland Stanford Junior University, The Stanford University  
450 Serra Mall  
Stanford, CA 94305-2004**

**3 September 2019**

**Final Report**

**APPROVED FOR PUBLIC RELEASE: DISTRIBUTION IS UNLIMITED.**



**AIR FORCE RESEARCH LABORATORY  
Space Vehicles Directorate  
3550 Aberdeen Ave SE  
AIR FORCE MATERIEL COMMAND  
KIRTLAND AIR FORCE BASE, NM 87117-5776**

# DTIC COPY

## NOTICE AND SIGNATURE PAGE

Using Government drawings, specifications, or other data included in this document for any purpose other than Government procurement does not in any way obligate the U.S. Government. The fact that the Government formulated or supplied the drawings, specifications, or other data does not license the holder or any other person or corporation; or convey any rights or permission to manufacture, use, or sell any patented invention that may relate to them.

This report is the result of contracted fundamental research which is exempt from public affairs security and policy review in accordance with AFI 61-201, paragraph 2.3.5.1. This report is available to the general public, including foreign nationals. Copies may be obtained from the Defense Technical Information Center (DTIC) (<http://www.dtic.mil>).

AFRL-RV-PS-TR-2019-0134 HAS BEEN REVIEWED AND IS APPROVED FOR PUBLICATION IN ACCORDANCE WITH ASSIGNED DISTRIBUTION STATEMENT.

//signed//

---

THOMAS LOVELL  
Program Manager

//signed//

---

DAVID WILT  
Tech Advisor, Space Component Technology  
Branch (Acting)

//signed//

---

JOHN BEAUCHEMIN  
Chief Engineer, Spacecraft Technology Division  
Space Vehicles Directorate

This report is published in the interest of scientific and technical information exchange, and its publication does not constitute the Government's approval or disapproval of its ideas or findings.

<b>F9DCFH8C7I A9BH5HCB'D5; 9</b>						Form Approved OMB No. 0704-0188	
U' a[BA^][ i q ^ / h ^ i a ^] A i A o B i j l ^ 8 d } A - H + i { z s d } A A * d a e a b i A e g ^ a s ^ A F a @ ^ I A ^ A n * [ ] ) • ^ E s y ^ a q ^ A o A q ^ A i : A n c a , q ^ / h * d ^ 8 d } • E ^ a s 8 q ^ A c a q ^ / A z a z a [ ^ i s ^ E s a o i a ^ A q a A z s s q a ^ A o o A z a z a ^ A a n a B e g a B i [ ] j l q ^ A e g a A n c a , q ^ / A o B i j l ^ 8 d } A - H + i { z s d } B U ^ ) a B i [ ( ^ ) o A ^ a s a ^ A o B i : i a ^) A * d a e a b i A e g ^ a s ^ A F a @ ^ I A ^ A n * [ ] ) • ^ E s y ^ a q ^ A o A q ^ A i : A n c a , q ^ / h * d ^ 8 d } • E ^ a s 8 q ^ A c a q ^ / A z a z a [ ^ i s ^ E s a o i a ^ A q a A z s s q a ^ A o o A z a z a ^ A a n a B e g a B i [ ] j l q ^ A e g a A n c a , q ^ / A o B i j l ^ 8 d } A - H + i { z s d } B i s y ^ a q ^ A o A q ^ A i : A n c a , q ^ / h * d ^ 8 d } • E ^ a s 8 q ^ A c a q ^ / A z a z a [ ^ i s ^ E s a o i a ^ A q a A z s s q a ^ A o o A z a z a ^ A a n a B e g a B i [ ] j l q ^ A e g a A n c a , q ^ / A o B i j l ^ 8 d } A - H + i { z s d } X O G G C E F A H E G B U ^ ) [ ] a ^ ) o A @ ^ i a B ^ A e g a s ^ A A z a z a [ q a o z s a q ^ A e g ^ A o B i : i c a q ^ ) A - A e g B i [ A ^ ) [ ] A o B i A e g ^ A a b 8 o B i A e g ^ A ^ ) a d A i : A e s q ^ A e B i [ ] j l A o B i j l ^ 8 d } A - H + i { z s d } A u A i ^ A [ o a a ] a s A e g ^ i i ^ ) q ^ A z a z a A U T O ^ B i ) d [ A ^ { a ^ i B D @ 5 G 9 ^ 8 C ^ B C H F 9 H I F B M C I F : C F A ^ H C ^ H c 9 ^ 5 6 C J 9 ^ 5 8 8 F 9 G G ^ "							
%F9DCFH85H9`'(DD-MM-YYYY) 03-09-2019			&'F9DCFH'HMD9 Final Report			' "85H9G7CJ9F98`'(From - To) 07 Mar 2016 – 03 Sep 2019	
( "HH@ `5B8`GI 6HH@						)U7'CBHF57'HBI A69F`	
Improved Dynamics Modeling of Proximity Flight using Relative Orbit Elements						)V"; F5BH'BI A69F` FA9453-16-C-0029	
						)WDFC; F5A`9@A9BHBI A69F` 61102F	
*"5I H<CFfGL Simone D'Amico and Riccardo Bevilacqua						)X"DFC>97'HBI A69F` 8809	
						)Y"H5G?`BI A69F` PPM00016414	
						)Z'K CF?'I B'HBI A69F` EF127130	
+"D9F: CFA-B; `CF; 5B-N5HCB'B5A9fgL5B8`588F9GGf9GL5B8 588F9GGf9GL Leland Stanford Junior University, The Stanford University 450 Serra Mall Stanford, CA 94305-2004						,"D9F: CFA-B; `CF; 5B-N5HCB'F9DCFH BI A69F	
-"GDCBGCF-B; `#ACB-HCF-B; `5; 9B7MB5A9fgL5B8`588F9GGf9GL Air Force Research Laboratory Space Vehicles Directorate 3550 Aberdeen Ave., SE Kirtland AFB, NM 87117-5776						% \$"GDCBGCF#A CB-HCFB57FCBMA fGL  AFRL/RVSV  %%"GDCBGCF#A CB-HCFB57F9DCFH BI A69FfGL AFRL-RV-PS-TR-2019-0134	
%&"8-GHF-6I HCB`#5J5-@6-@HMGH5H9A9BH Approved for public release: distribution is unlimited.							
% "GI DD@A9BH5FMBCHG							
% "56GHF57H The proposed research responds to the pressing need of the Air Force to better understand and utilize the dynamics of satellite relative motion for close-proximity missions. Current closed-form relative dynamics models are typically ad-hoc, mission-specific, and affected by major limitations such as the inter-satellite range of applicability, the eccentricity of the satellites orbits, the type of modelled perturbation forces, the resulting algorithm complexity and computational load. The project goal is to develop novel, efficient and accurate relative dynamics models for proximity operations that can be effectively used for orbit design, and guidance, navigation and control (GN&C) in a broad range of mission scenarios. Those scenarios include orbits of arbitrary eccentricity at small to large distances from Earth (e.g., from low-Earth to geostationary orbits) and with inter-spacecraft separations from virtually zero to hundreds of kilometers.							
% "GI 6>97HH9FAG Relative motion, Proximity operations, Formation-Flying, Dynamics, Guidance, Navigation, Control, Relative Orbit Elements, Gauss Variational Equations							
% "G97I F-HM7 @GG- =75HCB'C: .				% "@A-H5HCB C: `56GHF57H	% "BI A69F C: `D5; 9G	% U"B5A9`C: `F9GDCBG-6 @`D9FGCB` Dr. Thomas Lovell	
U'F9DCFH Unclassified	V"56GHF57H Unclassified	WHk-G'D5; 9 Unclassified	SAR		54	19b. TELEPHONE NUMBER %pmf g'ttgc" edf g+ (505) 843-4132	

**(This page intentionally left blank)**

## TABLE OF CONTENTS

Section	Page
List of Figures .....	iii
List of Tables .....	v
1.0 SUMMARY .....	1
2.0 INTRODUCTION.....	2
3.0 METHODS, ASSUMPTIONS, AND PROCEDURES .....	3
3.1 SURVEYS .....	3
3.1.1 Dynamics Models .....	3
3.1.2 GN&C Requirements.....	3
3.2 DYNAMICS.....	4
3.2.1 Linear Dynamics Models.....	4
3.2.2 Second Order Dynamics Models. ....	5
3.3 GUIDANCE .....	6
3.3.1 Swarming.....	6
3.3.2 Integration Constants as State Variables.....	8
3.3.3 Input Shaping Approach.....	8
3.4 CONTROL .....	10
3.4.1 Impulsive Control.....	10
3.4.1.1 Closed-form Solutions Approach.....	10
3.4.1.2 Numerical Algorithm.....	11
3.4.2 Continuous Control.....	12
3.4.2.1 Spirals Approach.....	12
3.4.2.2 ROE Approach.....	13
3.5 NAVIGATION.....	15
3.5.1 Angles-only Navigation.....	15
3.6 HIGH FIDELITY VALIDATION.....	16
3.6.1 Stanford's SLAB Robotic Testbed.....	16
3.6.2 University of Florida ADAMUS Lab Robotic Testbed.....	17

4.0	<b>RESULTS AND DISCUSSION</b>	19
4.1	<b>SURVEYS</b>	19
4.1.1	Dynamics Models	19
4.1.2	GN&C Requirements	19
4.2	<b>DYNAMICS</b>	21
4.2.1	Linear Dynamics Models	21
4.2.2	Second Order Dynamics Models	23
4.3	<b>GUIDANCE</b>	24
4.3.1	Swarming	24
4.3.2	Integration Constants as State Variables	26
4.3.3	Input Shaping Approach	27
4.4	<b>CONTROL</b>	29
4.4.1	Impulsive Control	29
4.4.1.1	Closed-form Solutions Approach	29
4.4.1.2	Numerical Algorithm	30
4.4.2	Continuous Control	31
4.4.2.1	Spirals Approach	31
4.4.2.2	ROE Approach	32
4.5	<b>NAVIGATION</b>	34
4.5.1	Angles-only Navigation	34
4.6	<b>HIGH FIDELITY VALIDATION</b>	36
4.6.1	Stanford's SLAB Robotic Testbed	36
4.6.2	University of Florida ADAMUS Lab Robotic Testbed	38
5.0	<b>CONCLUSIONS</b>	39
6.0	<b>REFERENCES</b>	40

# LIST OF FIGURES

Figure		Page
Figure 1:	Contour plot of time-averaged relative acceleration due to differential atmospheric drag vs orbit perigee altitude and eccentricity.....	5
Figure 2:	Relationships among prominent translational-state relative motion solutions for unperturbed orbits, emphasizing the new solution's derivation procedure.....	6
Figure 3:	Block diagram demonstrating the control implementation approach for swarming.....	7
Figure 4:	Modeling Approach using Integration Constants.....	8
Figure 5:	Reachable sets in the projected rel. mean longitude, rel. semi-major axis (left), relative eccentricity vector (middle), and relative inclination vector (right) planes.....	11
Figure 6:	Illustration of optimality condition where the dual variable ( $\lambda$ ) is an outward normal direction to the reachable set (red) at the target state (black sphere).....	12
Figure 7:	Selection of relative spiral trajectories in the radial-transverse plane of the chief spacecraft..	13
Figure 8:	Illustration of relationship between range ( $\delta\lambda$ ) and average elevation angle .....	16
Figure 9:	Computer-aided design drawing of the OS (top) and photograph of the OS (bottom).....	17
Figure 10:	ADAMUS testbed.....	18
Figure 11:	Electrical and data architecture of testbed.....	18
Figure 12:	Propagation accuracy of relative motion models in literature compared to numerically integrated ground truth including $J_2$ - $J_5$ .....	19
Figure 13:	Combined effects of Keplerian relative motion, $J_2$ , and differential drag on ROEs in eccentric orbits.....	22
Figure 14:	Evolution of the in-plane density-model-free STM propagation errors for highly eccentric orbit test with a Jacchia–Gill atmosphere.....	22
Figure 15:	Relative eccentricity vector circulation in near-circular Earth equatorial orbit due to SRP (eclipses neglected).....	23
Figure 16:	Monte Carlo analysis varying the nominal chief orbit inclination of the formation in geostationary orbit: quasi-nonsingular state (left) and nonsingular state (right). Detailed views (bottom).....	23
Figure 17:	Maximum position error over 10 orbits using a range of eccentricities for a selection of translational state solutions compared to a Keplerian truth.....	24
Figure 18:	The error in ROE space of each deputy satellites over time, where the error is defined as the difference between the current and the goal ROE to attain the desired swarm formation.....	26
Figure 19:	Optimal motion planning problem in Integration Constants space (left) and operative Cartesian space (right).....	27
Figure 20:	Guidance and nonlinear trajectories given by ZVD shaper for Case 2 ( $\alpha = 45^\circ$ ) .....	28
Figure 21:	Optimized trajectories given by ZVD shaper for Case 2.....	28
Figure 22:	Reachable sets in the projected rel. mean longitude, rel. semi-major axis (left) and relative eccentricity vector (right) planes.....	29

Figure 23: Evolution of the ROE in the 2D projected planes propagated with maneuvers under full-force dynamics model.....	30
Figure 24: Required refinement iterations for convergence to a solution with a cost within one percent of the global optimum for 1000 example problems.....	31
Figure 25: Comparison of formation acquisition trajectories using relative spirals with continuous-thrust and Hohmann transfers with impulsive maneuvers.....	32
Figure 26: Simulation setup for the validation of proposed control strategies.....	32
Figure 27: Example reconfiguration with wall constraints for a chief-deputy pair in a near-circular, retrograde low earth orbit.....	34
Figure 28: Evolution of estimation error for batch relative orbit determination after each regularized batch least squares iteration for example test scenario.....	35
Figure 29: Evolution of state estimation errors (solid lines) and 3-sigma formal covariance (shaded regions) from numerical UKF using modeled measurements for three targets at different ranges including eclipses (gray bars).....	36
Figure 30: Architecture of hardware-in-the-loop AON algorithm.....	37
Figure 31: OS images during AON trials. Both SOs and NSOs are present, with the target NSO outlined in red.....	37
Figure 32: ROE estimation errors from the UKF. Vertical gray bars represent periods of eclipse.....	38
Figure 33: Projection of guidance and robotic testbed tracking on ADAMUS testbed.....	39
Figure 34: ADAMUS testbed reference tracking position and velocity error.....	39



## LIST OF TABLES

Table	Page
Table 1. Temporal distribution and magnitudes of impulses for ZV and ZVD.....	9
Table 2. Shaped control command through ZV and ZVD.....	9
Table 3. Summary of analytical and semi-analytical continuous control solutions.....	14
Table 4. Qualitative comparison between PSO and MILP approaches.....	15
Table 5. Relative orbit control accuracy and mean inter-satellite distance for objective-related class of formation flying missions.....	20
Table 6. Relative navigation accuracy for objective-related class of FF missions.....	21
Table 7. Results of the control algorithm implementation for a swarm in a near-equatorial, near- circular orbit with a 450 km altitude simulated for 10 weeks.....	25
Table 8. Initial state $\mathbf{x}_0$ or studied cases.....	27
Table 9. Initial mean orbital elements of the observer.....	36
Table 10. Mean ROE for the test case.....	36
Table 11. Initial mean chief orbit in Keplerian orbital elements.....	38
Table 12. Relative orbit at the initial and final maneuver time.....	38

--- Vj k'Rci g'Kvqpvkpcmf 'Ngh'Diepm---

## 1.0 SUMMARY

The developed research responds to the pressing need of the Air Force to better understand and utilize the dynamics of satellite relative motion for close-proximity missions. Current closed-form relative dynamics models are typically ad-hoc, mission-specific, and affected by major limitations such as the inter-satellite range of applicability, the eccentricity of the satellites orbits, the type of modelled perturbation forces, the resulting algorithm complexity and computational load. The *project goal* is to develop novel, efficient and accurate relative dynamics models for proximity operations that can be effectively used for orbit design, and guidance, navigation and control (GN&C) in a broad range of mission scenarios. Those scenarios include orbits of arbitrary eccentricity at small to large distances from Earth (e.g., from low-Earth to geostationary orbits) and with inter-spacecraft separations from virtually zero to hundreds of kilometers. Closed-form solutions of the general and linearized equations of relative motion are sought, including all relevant perturbations acting at those orbit regimes. The perturbations include zonal harmonics of the Earth's geo-potential, third body forces from Sun and Moon, differential drag and solar radiation pressure, as well as control forces from impulsive and continuous maneuvering. The following *research objectives* have been pursued: (a) investigate novel relative dynamics models for proximity operations missions characterized by higher accuracy, range of applicability, and computational efficiency as compared with the state-of-the-art; (b) derivate closed-form analytical solutions of the equations of relative motion that account for the representative forces acting on proximity missions in low- and high-Earth orbits of arbitrary eccentricity; (c) derivate and apply state transformations for the new solutions of the relative dynamics which allow analysis, visualization, and manipulation of the relative motion models in a simpler domain based on non-singular relative orbit elements; (d) demonstrate how the newly derived solutions bring significant advantages to orbit design, GN&C of spacecraft for proximity operations missions; and, (e) validate rigorously the derived models through numerical integration, flight data from real proximity operations missions, and hardware-in-the-loop experimental tests in high-fidelity laboratories at Stanford University and the University of Florida. The *research objectives* are accomplished through the adoption of a state representation in terms of non-singular relative orbit elements (ROE). The non-homogeneous equations of the relative motion can be more easily solved using this proposed state representation and the method of variations of parameters (e.g., Gauss Variational Equations). In addition, a novel general nonlinear mapping allows transformation from the relative orbit element space to the more traditional Hill's space of position and velocity coordinates. *Four important outcomes have been achieved. First*, the development of a new closed-form solution of the general equations of relative motion (non-linearized) and the extension of the PI's theory of eccentricity/inclination vector separation to orbits of arbitrary eccentricity, a required step to improve the design of future missions. *Second*, the inclusion of all relevant perturbations found at high orbit altitudes (e.g., above geostationary orbits or high elliptic orbits). *Third*, the derivation of new, more accurate state transition, measurement input, and control input matrices for relative orbit dynamics and GN&C, valid for eccentric orbits and suitable for on-board implementation. *Fourth*, the development of more efficient control techniques in terms of relative

orbit elements that fuse input shaping and primer vector theory. The developed research *significantly impacts Air Force Research Laboratory capabilities* by maintaining U.S. space superiority and developing key knowledge needed to efficiently design, implement, and operate proximity operations missions of strategic relevance. The project leveraged the PIs' unique experience and qualifications to understand and identify the requirements on theoretical modeling for spacecraft dynamics in proximity missions. The PI, Dr. Simone D'Amico, is at the forefront in the design and implementation of advanced algorithms for spacecraft formation-flying and on-orbit servicing, has provided key contributions to the few currently operational spacecraft formation-flying missions, and developed the ROE-based concept of relative eccentricity/inclination vector separation, which is the backbone of the GN&C design of dual-satellite missions such as GRACE (U.S.), PRISMA (Sweden), TanDEM-X and DEOS (DLR), PROBA-3 (ESA). Co-PI, Dr. Riccardo Bevilacqua, has been awarded two young investigator awards (AFOSR, 2012; ONR, 2013), and has extensive experience in propellant-free spacecraft relative maneuvering (see PADDLES mission concept), differential drag modeling, state estimation, and hardware-in-the-loop experimentation for spacecraft formation-flying.

## 2.0 INTRODUCTION

This research addresses the most general spacecraft formation, which consists of two or more objects flying in close proximity, either cooperatively or non-cooperatively, in elliptic perturbed orbits. "Close proximity," means that the relative motion between the objects can be linearized about the reference orbit, which can be either the physical orbit of one of the objects or a virtual orbit. "Formation," without loss of generality, is assumed to consist of two satellites, namely the chief and the deputy. The "chief" defines the reference orbit and is uncontrolled (or passive), whereas the "deputy" is controlled by a three-dimensional thrust input (or active). The formalism adopted in this work allows a seamless exchange of roles between chief and deputy, or the treatment of an arbitrary number of deputies.

Given this general framework, the main advances presented in this report are listed in the following:

1. Harmonization of the state-of-the-art in dynamic modelling [1] and GN&C requirements [2] through peer reviewed surveys and comparative assessments.
2. Development of linear dynamics models of unprecedented accuracy for the propagation of the spacecraft relative motion in closed-form [3] [4] [5].
3. Development of second order dynamics models including eccentricity and J2-effects [6].
4. Extension of the relative eccentricity inclination vector separation concept to  $N$ -spacecraft swarms [7] [8].
5. Generalization of the concept of integration constants as state variables for optimal path planning of systems governed by ordinary differential equations [9].
6. Development of guidance approach using input shaping [10].

7. Development of new closed-form impulsive control solutions [11][12].
8. Development of new numerical algorithm for impulsive control of linear time variant systems [13].
9. Low thrust control approaches using spirals [14] [15], and relative orbital elements [16][17][18][19][20].
10. Development of angles-only navigation filtering pipeline leveraging relative orbital elements with minimal a-priori info [21] [22] [23] [24].
11. Development of high-fidelity validation testbeds at Stanford's Space Rendezvous Laboratory [25][26][27] and at University of Florida's ADAMUS Lab [28].

In the following sections, these advances are summarized and linked to the corresponding published articles and overall contract research objectives.

### **3.0 METHODS, ASSUMPTIONS, AND PROCEDURES**

#### **3.1 SURVEYS**

##### **3.1.1 Dynamics Models**

Closed-form models of spacecraft relative motion have found many valuable applications in both onboard guidance, navigation, and control (GN&C systems and offline mission-planning analysis. However, models available in literature exhibit widely varying constraints and limitations on their range of applicability (inter-satellite separation, eccentricity, and modeled perturbations, accuracy, and computation cost. Additionally, these models use diverse state definitions based on Cartesian position and velocity, Keplerian orbital elements, or other parameters. Due to these differences, it can be difficult to establish a benchmark to determine which dynamics models are best suited for a given mission scenario. To facilitate such decisions, an extensive survey of closed-form dynamics model in literature was conducted [1]. Particular attention was paid to the dynamical state representation, the immediate assumptions on the model, the types of perturbations included, and the provided metrics on accuracy and computational complexity. A comparative assessment of a subset of these models was conducted to provide quantitative performance metrics subject to consistent test conditions that are representative of relative motion scenarios of formation-flying missions. This assessment was used to rigorously characterize the accuracy of these models with respect to key parameters such as orbit size, eccentricity, and inter-spacecraft separation.

##### **3.1.2 GN&C Requirements**

The main challenge related to spacecraft formation flying missions is the design of robust and reliable GN&C techniques for onboard systems. In light of this, a comprehensive survey of formation-flying missions have been conducted in order to determine the state-of-the-art of onboard GN&C subsystem in terms of technologies (hardware and software) and achievable

performances, and 2 to define the requirements for GN&C subsystem design in accordance with the new technology trends. Formation-flying missions already launched or planned to be have been reviewed, spanning the space programs from 2000 to 2025. The survey has included missions designed by national space agencies, government R&D centers or scientific agencies, universities, and private companies spread out all around the world (see [2] for more details. Missions have been classified based on 1 *mission objective*, 2 *satellite mass*, and 3 *orbital regime*, and GN&C requirements have been derived accordingly. The survey of dynamics models and GN&C requirements has informed the research conducted in this project and motivated the developments described in the next sections.

## 3.2 DYNAMICS

### 3.2.1 Linear Dynamics Models

Linear dynamics models of the spacecraft relative motion affected by orbital perturbations are well known in literature and have been extensively exploited in real space missions. This work [3] [4] [5] expands over the state-of-the-art by developing new linear dynamics models which fulfill orbit propagation accuracy requirements needed by on-board GN&C algorithms in a multitude of orbit scenarios as discussed in the previous section. The new models are derived through a general methodology which fosters the inclusion of both conservative and non-conservative perturbations. The inclusion of non-conservative perturbations is important because these phenomena have significant impact on the evolution of the relative motion of a formation in commonly used orbits (see Figure 1. The proposed derivation methodology includes three steps. First, the state is augmented by force model parameters. Second, a Taylor expansion on the equations of relative motion including secular and long-periodic effects of the most relevant perturbations is performed. Finally, closed-form solutions of the resulting linear differential equations are computed. The obtained linear models are presented for a variety of state representations based on so-called Relative Orbital Elements (ROE: nonsingular, quasi-nonsingular, and singular. The perturbations included in the linear models are: gravity potential effects J2 [3][4][5] and J3 [4], atmospheric drag [3], solar radiation pressure [4][5], and third body gravity from the sun and moon [4]. The variety of perturbations included in the new models extend their applicability to a multitude of orbit scenarios: from near-circular Low Earth Orbit [3] to Highly Eccentric Earth Orbits (e.g., Telescopy Orbits [3] and Geostationary Transfer Orbits [4] [5] and near-circular Geostationary Orbits [4] [5], all the way to orbits around near-Earth asteroids in eccentric orbits around the Sun [5]. In addition, the new linear models provide geometric insight on the effect of these perturbations on the ROE. This is considered for efficient formation-flying control and guidance as discussed in the next sections.

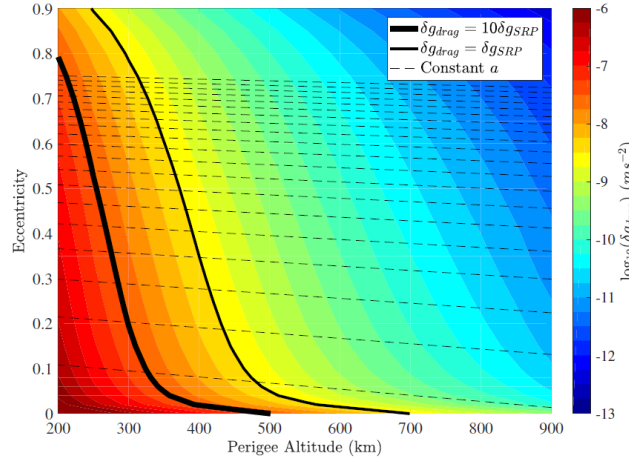


**Figure 1: Contour plot of time-averaged relative acceleration due to differential atmospheric drag vs orbit perigee altitude and eccentricity with comparison to time-averaged relative acceleration from solar radiation pressure (black lines)**

### 3.2.2 Second Order Dynamics Models

The survey of closed-form dynamics models revealed a gap in the literature. Solutions exist for linear dynamics on near-circular and eccentric orbits, as well as for second- and higher-order dynamics on near-circular orbits, but higher-order translational state solutions applicable to eccentric orbits had not been proposed. This prompted the development of a new, second-order solution for the relative position and velocity of two spacecraft on orbits of any eccentricity [6]. The new solution was created under the assumption of unperturbed, Keplerian motion using the method of successive approximations. After series expanding the differential gravitational attraction and truncating at second order in inter-satellite separation, the equations of motion were transformed to a nondimensional form through normalization by the orbit radius and change of independent variable from time to true anomaly. Dropping the nonlinear terms leaves a linear, homogeneous system whose solution is known. An approximate solution to the nonlinear system is then found by substituting the linear solution into the second-order terms to produce a linear, inhomogeneous system that may be solved by the variation of parameters technique. The new solution unifies several translational state solutions from the literature and reduces to those as eccentricity or inter-satellite separation are reduced to zero (Figure 2).

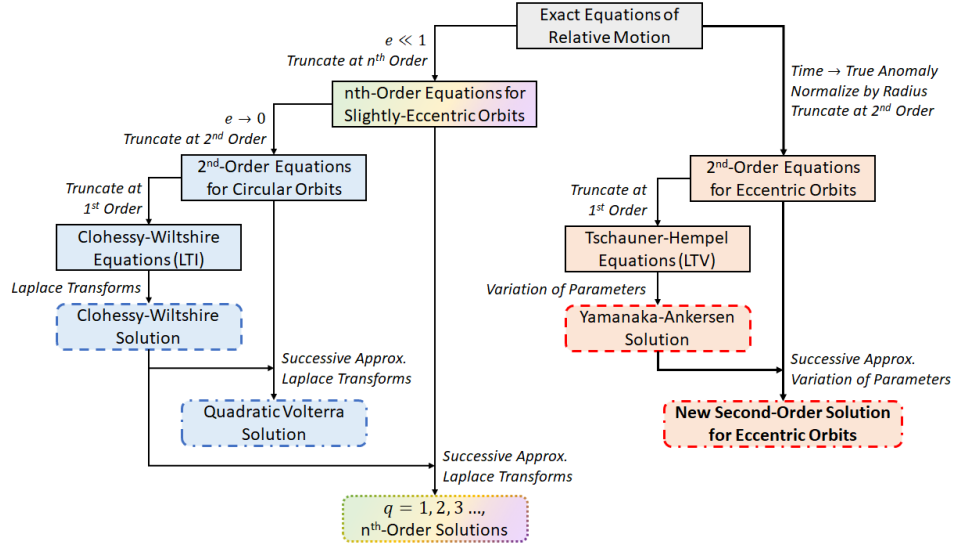


**Figure 2: Relationships among prominent translational-state relative motion solutions for unperturbed orbits, emphasizing the new solution’s derivation procedure**

### 3.3 GUIDANCE

#### 3.3.1 Swarming

Spacecraft swarms enable novel future missions through distributed sensing capabilities with example applications of distributed antennas or sparse aperture arrays. As an added benefit, swarms provide inherent fault tolerance compared to monolithic spacecraft due to the large number of identical spacecraft that constitute a swarm. However, available literature for keeping the formation geometry of multiagent systems focuses on robotic applications that assume simple dynamics, significant computational resources, and unlimited control authority. These approaches are unsuitable for the complex orbital dynamic environment and limited resources (computational and fuel) aboard the small swarm spacecraft. Furthermore, literature lacks an analysis of initial swarm mission phases, specifically deployment, as focus has been on the safe deployment of binary formations. Compared to swarms, the deployment of a binary formation is less challenging due to the smaller number of spacecraft involved which results in simpler collision avoidance. These limitations in swarm guidance were overcome through the development of swarm geometries and formation-keeping algorithms designed for the realistic space environment in [7] and a safe deployment scheme of the aforementioned geometries in [8].

These works leverage ROE to produce simple constraints for safety and computationally efficient state-space control algorithms by exploiting known, natural dynamics for Earth orbits produced by available STMs [3,4]. For formation keeping, the use of mean ROE enabled the derivation of analytical constraints that guarantee swarm safety and a minimum delta-v usage. Specifically, a minimum delta-v usage was achieved by requiring active control only during periods where



passive safety was absent; exploiting the dynamic environment for differential drag control; and leveraging known minimum delta-v maneuvers in ROE space [11, 12]. For acquisition and deployment, uncertainties in launch direction and delta-v were cast into regions of accessibility in ROE space. By leveraging known dynamics of the reachable relative orbits by deployment, constraints on the injection errors and limits on the commissioning phase to guarantee satellite safety are derived. With these limitations, a deployment approach and maneuver sequence of the mothership are presented that guarantee swarm safety given uncertainties in deployment and commissioning phase requirements. Validation of the formation-keeping algorithms and deployment schemes in a realistic mission scenario demonstrate the algorithms' capabilities. The pipeline of these simulations is shown in Figure 3. The top subfigure demonstrates the numerical formulation of the mean ROE. The bottom subfigure of Figure X demonstrates the approach starting with the generation of the ground truth, including representative measurement noise, and ending at the control law logic that generates the maneuvers to be implemented.

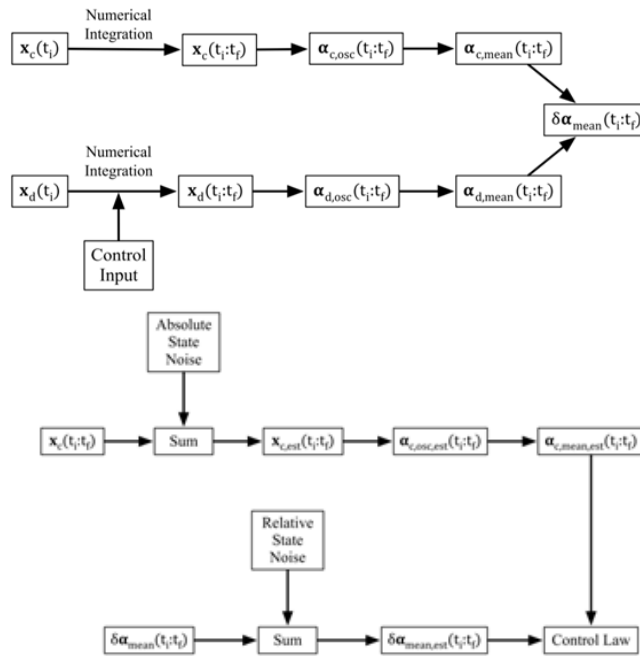


**Figure 3. Block diagram demonstrating the control implementation approach for swarming. The top subfigure demonstrates how the mean ROE are produced from ground-truth data with noise representative of sensor data. The bottom subfigure demonstrates how both the mean absolute and relative orbit state are used in the control logic to produce an executable maneuver**

### 3.3.2 Integration Constants as State Variables

[9] explores the advantages of a state parameterization in integration constants to optimally path plan multi-dimensional systems governed by ordinary differential equations. The idea is inherited from astrodynamics, where the integration constants of the unperturbed equations of orbital motion – orbital elements – are used to path plan optimally artificial satellites in space. This paper shows that the advantages gained from this state parameterization can be generalized to potentially any multi-dimensional systems governed by ordinary differential equations. The approach is the following: firstly, the original non-integrable multi-dimensional system of ODE (Fig. 4, top left) is reduced to a simpler integrable form in the operative state variables (Fig. 4, bottom left), secondly, a closed form map allows to recast the reduced system in IC-state space (Fig. 4, bottom right), thirdly, a new set of first order differential equations govern the evolution of the new IC state parameters (Fig. 4, top right).

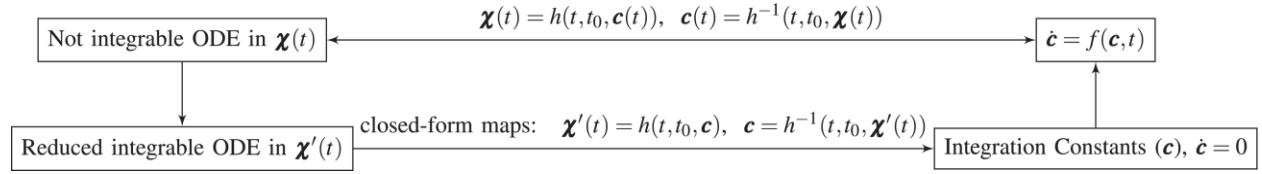


**Figure 4. Modeling Approach using Integration Constants**

Using this approach, [9] shows that working in integration constant space simplifies the path planning. In particular, the integrable dynamics can be exploited intrinsically, while the part of the dynamics which is not integrable can be isolated and compensated.

### 3.3.3 Input Shaping Approach

In the frame of this study, input-shaping approach has been proposed to derive guidance solutions to the problems of short-distance planar spacecraft re-phasing and rendezvous when continuous low thrust is used. The main idea of the input-shaping method is based on the convolution of the command signal with a sequence of Dirac impulses. These impulses must be applied in specified moments of time,  $T_i$ , and with specified amplitude,  $A_i$ , in order to nullify the residual vibrations of the system, [10]. Two classes of shapers, namely, the zero vibration (ZV) and the zero vibration derivative (ZVD), have been investigated, consisting of two and three impulses, respectively, with the temporal distribution and magnitudes listed in Table 1.

**Table 1. Temporal distribution and magnitudes of impulses for ZV and ZVD**

<i>Shaper</i>	<i>Impulses Temporal Distribution</i>	<i>Impulses Magnitude<sup>1</sup></i>
Zero vibration	$T = [0, \Delta t]$	$A = \left[ \frac{\zeta}{\zeta + 1}, \frac{1}{\zeta + 1} \right]$
Zero vibration derivative	$T = [0, \Delta t, 2\Delta t]$	$A = \left[ \frac{\zeta^2}{\zeta^2 + 2\zeta + 1}, \frac{2\zeta}{\zeta^2 + 2\zeta + 1}, \frac{1}{\zeta^2 + 2\zeta + 1} \right]$

For the purpose of deriving the control profile for the in-plane deputy maneuvering, the aforementioned shapers have been used to shape a bang–bang continuous command of amplitude  $\bar{u}$ . Assuming that the control vector,  $\mathbf{U} = [u \sin(\alpha), u \cos(\alpha)]^T$ , is misaligned of an angle  $\alpha$  with respect to the y-axis direction of local reference frame, the shaped control command,  $u$ , has been computed by the expressions reported in Table 2.

**Table 2. Shaped control command through ZV and ZVD**

<i>Shaper</i>	
Zero vibration	$u = A_1 f_{t1} + A_2 f_{t2}$ $f_{t1} = \begin{cases} 0 & t > t^* \\ \bar{u} \operatorname{sign}(\bar{y}_d - y_0) & t < \frac{t^*}{2} \\ -\bar{u} \operatorname{sign}(\bar{y}_d - y_0) & \frac{t^*}{2} < t < t^* \end{cases}$ $f_{t2} = f_{t1}(t - \Delta t)$
Zero vibration derivative	$u = A_1 f_{t1} + A_2 f_{t2} + A_3 f_{t3}$ $f_{t1} = \begin{cases} 0 & t > t^* \\ \bar{u} \operatorname{sign}(\bar{y}_d - y_0) & t < \frac{t^*}{2} \\ -\bar{u} \operatorname{sign}(\bar{y}_d - y_0) & \frac{t^*}{2} < t < t^* \end{cases}$ $f_{t2} = f_{t1}(t - \Delta t)$ $f_{t3} = f_{t1}(t - 2\Delta t)$

The step-by-step process to determine the analytical guidance solution has been as follows. First, the expression for the in-plane final state,  $\mathbf{X}_f = [x_f, y_f, \dot{x}_f, \dot{y}_f]^T$ , and along-track location of the

<sup>1</sup>  $\zeta = e^{\pi\zeta/\sqrt{1-\zeta^2}}$ , where  $\zeta$  is the damping ratio of the relative dynamics system.

center of the final relative orbit,  $\bar{y} = y_f - \frac{2\dot{x}_f\bar{m}}{\bar{n}^2}$ , have been computed, assuming the shaped control signal  $u$  reported in Table 2 is applied. Given a desired along-track location of the center of the final relative in-plane orbit,  $\bar{y}_d$ , the expression of  $\bar{y}$  has been solved for the necessary bang-bang time,  $t^*$ , which results in  $\bar{y} = \bar{y}_d$  at the end of the maneuver. Then, the requirements to obtain a non-drifting close trajectory have been determined and the final relative eccentricity has been derived as a function of initial state,  $\mathbf{X}_0 = [x_0, y_0, \dot{x}_0, \dot{y}_0]^T$ , control parameters,  $\mathbf{p}_u = [\Delta t, \bar{u}, \alpha]$ , and dynamics parameters,  $\mathbf{p}_u = [\bar{n}, \bar{m}]$ .

The final relative state has been computed analytically taking advantage of the close-form solution of Schweighart-Sedwick (SS) linear dynamics model, which allows accounting for J2 perturbing effects. Ultimately, a gradient-based algorithm has been proposed to find the values of  $\Delta t$  and  $\alpha$  that minimize the maneuver cost,  $\Delta V = \bar{u}(t^*(\alpha) - \Delta t)$ , satisfying the following constraints

$$\begin{aligned} & |e_{rel,f}(\Delta t, \alpha) - e_{rel,f,d}| = 0 \\ & \begin{cases} \frac{t^*(\alpha)}{2} - 2\Delta T > 0 & \text{for ZVD} \\ \frac{t^*(\alpha)}{2} - \Delta T > 0 & \text{for ZV} \end{cases} \end{aligned} \quad (1)$$

where  $e_{rel,f,d}$  indicates the desired final relative eccentricity.

### 3.4 CONTROL

#### 3.4.1 Impulsive Control

##### 3.4.1.1 Closed-form Solutions Approach

Reference [12] uses reachable set theory to derive new solutions to satellite relative orbit reconfiguration problem of achieving a desired end state in fixed-time. The reachable set  $S^*(c, T)$  is defined as the geometric relative orbit element space that can be achieved in finite time  $T$  with multiple maneuvers of total cost  $c$  [12]. The reachable set scales linearly with cost. If the set is defined with the optimal delta-v cost for a given reconfiguration, the desired end state will lie on the boundary of  $S^*$ . This visual representation of optimality motivates the derivation of the  $\delta v_{min}$  which represents a quantifiable lower bound on the cost of a given reconfiguration. Reference [12] proves that the minimum delta-v required to achieve the entire desired reconfiguration cannot be less than the maximum of the set of minimum delta-vs required to achieve each 2D reconfiguration independently, which means that a 2n-D problem can be reduced to n 2D problems and analyzed

---

<sup>2</sup>  $\bar{m} = n_{ref}\sqrt{1 + k_{j_2}}$ ,  $\bar{n} = n_{ref}\sqrt{1 - k_{j_2}}$  with  $k_{j_2} = \frac{3}{8}J_2\frac{R_e^2}{r_{ref}^2}(1 + 3\cos(2i_{ref}))$ .  $r_{ref}$  is the radius of the circular orbit of the chief satellite,  $i_{ref}$  the inclination, and  $n_{ref}$  the chief rotational rate.

without loss of generality. For the 6D quasi-nonsingular ROE state representation, for a general eccentric orbit, reachable sets in the 3 2D planes are shown in Figure 5.

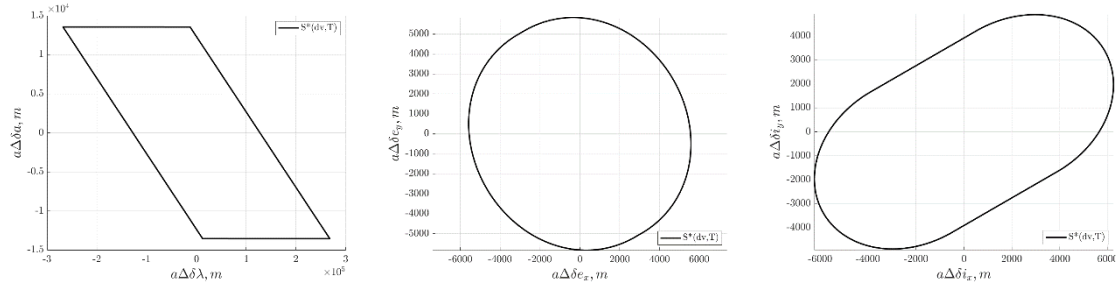


**Figure 5: Reachable sets in the projected rel. mean longitude, rel. semi-major axis (left), relative eccentricity vector (middle), and relative inclination vector (right) planes. The solid line is the boundary of the convex hull reachable with a total cost of 1 m/s**

The plane that drives the cost of the entire reconfiguration is called the dominant plane. First, reference [12] presents a general methodology to derive the  $\delta v_{min}$  and then applies it to the quasi-nonsingular ROE state representation to attain closed-form expressions for the  $\delta v_{min}$  for each dominance case. Second, the paper describes the general methodology used to derive optimal impulsive maneuver schemes that solve the satellite relative orbit reconfiguration problem. The paper also shows that the reachability of the  $\delta v_{min}$  for each dominance case is quantifiable by mapping the optimal times and maneuvers from the dominant plane into the non-dominant planes. Closed-form expressions for all maneuver schemes achievable with minimum delta-v are given explicitly.

### 3.4.1.2 Numerical Algorithm

Numerical algorithms for impulsive control of linear time-variant systems in literature are subject to significant limitations including limited radius of convergence and high computation cost. Additionally, these algorithms are often only applicable to simple cost functions such as p-norms. A more efficient and robust algorithm could find application in onboard maneuver planning and offline analysis of control algorithms. To meet this need, a new algorithm was developed that provides energy-optimal impulsive control inputs for fixed-time, fixed-end-condition control of linear time-variant systems [13]. The main novelty of the algorithm is that it accommodates time-varying norm-like cost functions, enabling inclusion of operational constraints (e.g. spacecraft attitude modes) in the maneuver planning problem. To facilitate the development of this algorithm, a new necessary and sufficient optimality condition is developed using reachable set theory. This condition is that the dual variable is an outward normal direction to the reachable set at the target state, as illustrated in Figure 6.

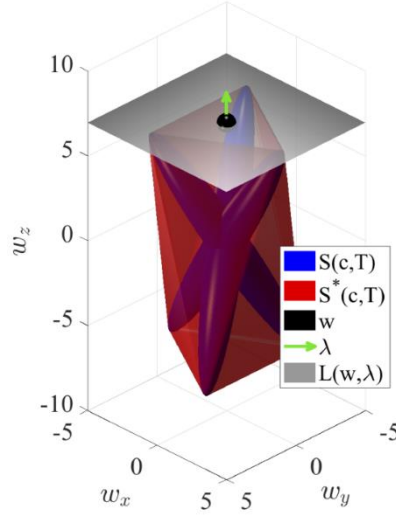


**Figure 6: Illustration of optimality condition where the dual variable ( $\lambda$ ) is an outward normal direction to the reachable set (red) at the target state (black sphere)**

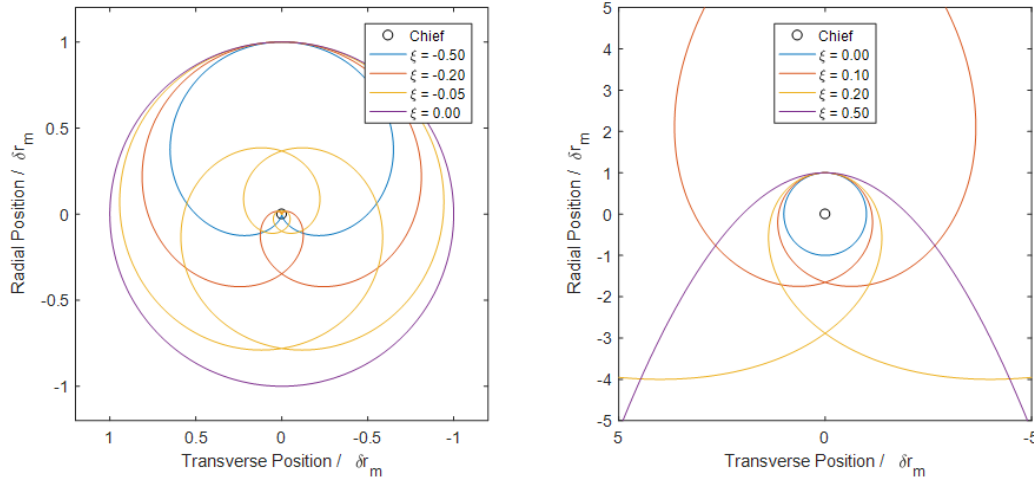
The proposed algorithm includes three steps: 1) generation of an initial set of control input times, 2) iterative refinement of the candidate control input times, and 3) extraction of optimal control inputs. The algorithm uses findings from reachable set theory to minimize computation cost and maximize robustness to numerical errors at every step. The accuracy and performance of the algorithm were characterized through Monte Carlo experiments with multiple initialization schemes. Additionally, the run time of the proposed algorithm was compared with two other state-of-the-art reference algorithms using direct and indirect optimization approaches.

### 3.4.2 Continuous Control

#### 3.4.2.1 Spirals Approach

Electric propulsion systems are of great interest for their high specific impulse but pose challenges for guidance and control due to the large design space created by the need for continuous low-thrust operation. Shape-based methods have been the subject of extensive study in the area of low-thrust trajectory design for the absolute motion of a single spacecraft. In such approaches, a spiral trajectory shape is introduced, and the equations of motion are used to derive the associated thrust profile. This leads to closed-form solutions for the trajectory, time-of-flight, thrust profile, and delta-v cost, and thereby simplifies the design and optimization problems. A novel strategy was introduced to apply shape-based methods to the problem of low-thrust formation flying through the use of relative spiral trajectories [14]. Using the equations of relative motion for near-circular orbits in a local polar coordinate system, analytical expressions were developed for the thrust, time-of-flight, and cost of following in-plane trajectories belonging to the family of sinusoidal spirals. The solutions are characterized by the tunable thrust parameter  $\xi$ , as illustrated in Figure 7. The conditions necessary to patch multiple spirals together were derived for the cases where both spirals use a common reference and where the reference changes across the patch. This makes

the approach highly flexible and allows greater freedom for optimization. The sensitivity of the approach to uncertainties in the state and thrust were evaluated using an open-loop implementation in a high-fidelity simulation environment [15].



Hli wt g'9<Uggevklp'qht gr vkg'lr kt cilt clgevqlgu'lp'vj g't cf kcn/vt cpuxgt ug't npg'qhl'vj g'ej kgh' ur ceget ch0Hqt 'vj g'ecug' ' >2'ighv+ 'vj g'gzvgpv'qhl'vj g't gr vkg'b qvklp'j cu'e'p'wr r gt 'dqwpf 0' Hqt 'vj g'ecug' ' @2't k j v+ 'vj g'gzvgpv'qhl'vj g't gr vkg'b qvklp'j cu'e'hy gt 'dqwpf "

## 50604TQG'Crrtqcej "

The spacecraft formation reconfiguration problem over a limited and defined interval of time by using finite-time maneuver strategies in near-circular J2-perturbed orbits has been investigated. The analytical and semi-analytical piecewise continuous control solutions for in-plane and out-of-plane reconfigurations have been derived by inverting the closed-form solution of relative dynamics, parameterized through the relative orbit elements. The general methodology used to obtain the continuous solutions consists of the following steps: 1) the expression of the final mean ROE state,  $\delta\alpha(T)$ , is derived through the state transition matrix and the convolution matrix associated with the linearized ROE-based dynamics model, 2) then, given a desired mean relative orbit,  $\delta\alpha_{des}$ , the expression  $\delta\alpha(T) = \delta\alpha_{des}$  is solved for the parameters that describe the control problem, i.e. the maneuvers' locations and amplitudes<sup>3</sup>. Two- and three-maneuver strategies have been analyzed for in-plane relative motion control, whereas a single cross-track maneuver is considered for the out-of-plane formation reconfiguration problem. As the aforementioned condition  $\delta\alpha(T) = \delta\alpha_{des}$  cannot be always solved analytically, some of proposed control strategies have been obtained using an iterative numerical algorithm (e.g. Brent's method) and, therefore, have been referred to as semi-analytical solutions. Table 3 briefly summaries the control strategies proposed for in-plane and out-of-plane problems, [17]. The full reconfiguration problem has been also investigated. More specifically, a control scheme consisting of three tangential finite-time maneuvers and one single out-of-plane maneuver has been proposed. In this case, the

<sup>3</sup> Note that the ROE state for in-plane problem is  $\delta\alpha_{ip}(t) = [\delta a(t), \delta\lambda(t), \delta e_x(t), \delta e_y(t)] \in \delta\alpha(t)$  and  $\delta\alpha_{oop}(t) = [\delta i_x(t), \delta i_y(t)] \in \delta\alpha(t)$

boundary condition  $\delta\alpha(T) = \delta\alpha_{des}$  is solved numerically through the Levenberg-Marquardt algorithm. It is worth remarking that the obtained solution takes into account the dynamics coupling between the in-plane and out-of-plane motion, even though it does not enable the minimization of the fuel consumption, [19]. "

**Vcdng'50'Uwo o ct { 'qhl'pcnf vlecn'lpf 'lgo k'pcnf vlecn'lpvlpwqwl'eqpv qnl' uqnlwkpul' "**

<i>Uqnlwkp"</i>	<i>Kp/rncpg't geqplki wtcvkqp" "rtqdrgo "'</i>	<i>Qww/ql/rncpg't geqplki wtcvkqp" rtqdrgo "'</i>
Analytical solution	<ul style="list-style-type: none"> <li>• Three-tangential maneuver strategy (T-T-T)</li> <li>• Two-radial/tangential maneuver strategy (RT-RT)</li> <li>• Two-radial maneuver strategy (R-R)</li> </ul>	None
Semi-analytical solution	<ul style="list-style-type: none"> <li>• Two-radial maneuver strategy (R-R)</li> </ul>	<ul style="list-style-type: none"> <li>• One-normal maneuver strategy (N)</li> </ul>

In addition, the design of minimum-fuel maneuvering scheme in J2-perturbed near-circular orbits has been addressed in the frame of this study. The reconfiguration problem has been formulated as an optimal control problem, assuming that the maneuverable spacecraft can perform only a series of constant finite-time maneuvers to control the relative configuration (i.e., the control acceleration profile is assumed to be a piecewise constant function over the maneuvering interval). Two different methods have been proposed to solve the aforementioned optimal control problem, namely the Mixed-Integer Linear Programming (MILP) approach and the Particle Swarm Optimization (PSO). The former requires the discretization of the maneuvering interval to cancel the nonlinearities related to the boundary conditions as well as the introduction of an additional set of optimization parameters to make the objective function linear, whereas the latter can directly solve the constrained nonlinear programming problem associated to the design of the minimum-fuel reconfiguration strategy. Collision avoidance and maneuvering time constraints dictated by mission operations have been considered to make the aforementioned approaches suited to handle the requirements coming from a realistic flight scenario. Linear dynamics model based on ROE parameterization and its associated closed-form solution is used to impose the boundary conditions, avoiding the dynamics integration within the optimization process. Table 4 shows a qualitative comparison between the two proposed numerical approaches.



**Table 4. Qualitative comparison between PSO and MILP approaches**

<i>Optimizer</i>	<i>Benefits</i>	<i>Drawbacks</i>
PSO	<ul style="list-style-type: none"> <li>• Easy transcription of the optimization problem</li> </ul>	<ul style="list-style-type: none"> <li>• Computing time demanding</li> <li>• It does not consider the number of maneuvers as a problem variable</li> </ul>
MILP	<ul style="list-style-type: none"> <li>• Computing time efficient</li> <li>• It includes the number of maneuvers as a problem variable</li> </ul>	<ul style="list-style-type: none"> <li>• It make the optimal problem transcription more complicated (increase of number of variable and constraints)</li> </ul>

An alternative approach has been proposed using Lyapunov based control in ROE space to accommodate constraints [20]. As opposed to previous approaches, the controller includes the  $J_2$  perturbation in the dynamic environment. Furthermore, by leveraging ROEs, the presented approach simplifies control computation in comparison to cartesian approaches.

### 3.5 NAVIGATION

#### 3.5.1 Angles-only Navigation

Angles-only navigation is a promising technology for applications in on-orbit servicing, space situational awareness, swarming, and formation flying missions. Angles-only navigation offers two main advantages over technologies such as LIDAR and GNSS navigation. First, it uses passive, low-cost sensors that are already ubiquitous on modern spacecraft. Second, it can be used for non-cooperative relative navigation with respect to debris or malfunctioning spacecraft.

The primary challenge of angles-only navigation is determining the range to the target object. Previous demonstrations of angles-only navigation rely on a common two-part recipe to resolve the range: 1) accurate a-priori information from the ground to initialize the filter, and 2) execution of maneuvers at regular intervals to improve observability via triangulation. However, future missions using small spacecraft in deep space may have limited contact with the ground and minimal maneuvering capability. As such, it is desirable to improve upon the state-of-the-art to enable angles-only navigation without requiring maneuvers or a-priori information.

To meet this need, two development efforts were conducted. First, a batch relative orbit determination algorithm was developed to provide an estimate of the relative state of a target object using only bearing angle measurements [21-24]. The developed algorithm includes three steps: 1) computation of a unit vector solution from a singular value decomposition of the observability

matrix, 2) computation of an initial estimate of the range using the average elevation angle (see Figure 8), and 3) iterative refinement using regularized least squares.

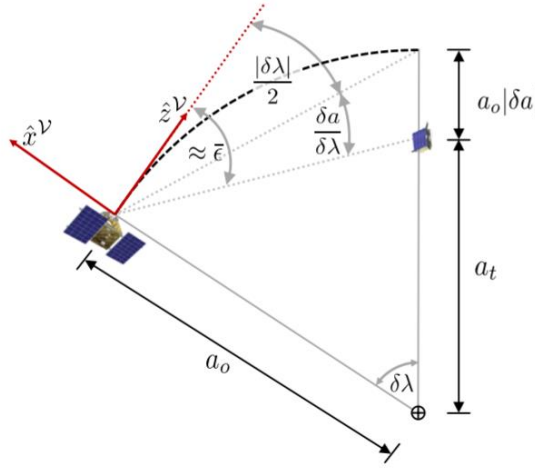


**Figure 8: Illustration of relationship between range ( $\delta\lambda$ ) and average elevation angle**

Second, a sequential filter architecture that enables reliable convergence to the true state without requiring translational maneuvers was developed [21-24]. The well-known weak observability of the problem was overcome by using an unscented Kalman filter (UKF), which does not require linearization of the measurement equations. Process noise is modeled using covariance matching over a sliding window, which allows the filter to be used a wide range of scenarios from low earth orbit to geosynchronous orbit. The developed filter architecture is compatible with analytical relative motion models (primarily the state transition matrices described in Section 3.2.1) and numerical integration of the equations of motion. The batch relative orbit determination algorithm and sequential filter were validated and characterized through extensive hardware-in-the-loop testing using the optical stimulator testbed.

### 3.6 HIGH FIDELITY VALIDATION

#### 3.6.1 Stanford's SLAB Virtual Reality Testbed

In order to rigorously validate the key vision-based GN&C algorithms for autonomous formation keeping, reconfiguration, and docking etc., the Stanford Space Rendezvous Laboratory has developed a virtual-reality hardware testbed – the Optical Stimulator (OS). The OS aims to synthetically replicate spaceborne images of a realistic space environment, which are used to stimulate a vision-based sensor (VBS) with illumination conditions as typically observed in earth orbit and deep space. The OS is a virtual reality testbed capable of creating and displaying synthetic images of non-stellar objects and a dynamic star field using OpenGL-based real-time rendering software. The software is able to render point sources of light spanning eight orders of magnitude in radiometric intensity with arcsecond-level angular precision. As shown in Figure 9, the OS

OLED monitor stimulates the VBS through a collimating optic (CO) formed from two lenses. These lenses can readily be moved or interchanged to achieve variable magnification, which allows testing of VBS with different fields of view; increases the dynamic range of the testbed; and may emulate inertial, far-range and close-range scenarios. Transitioning and mixed navigation regimes can therefore be tested.

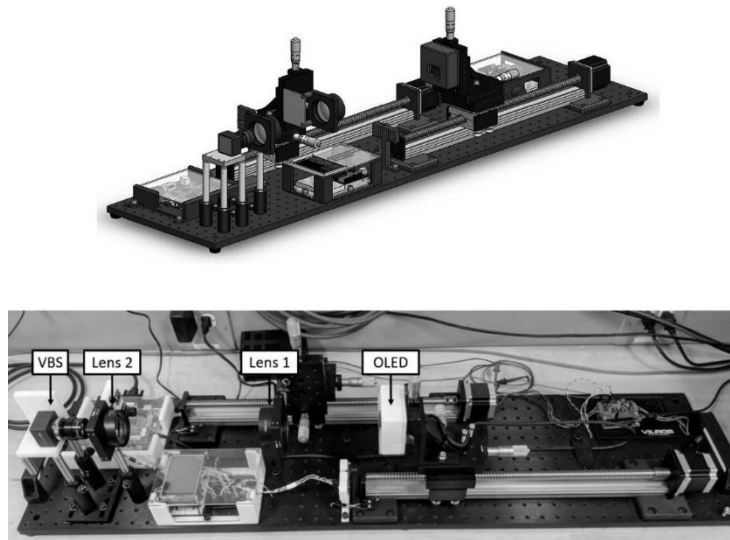


**Figure 9. Computer-aided design drawing of the OS (top) and photograph of the OS (bottom)**

### **3.6.2 University of Florida's ADAMUS Lab Robotic Testbed**

Accurate preflight testing environments for formation flying are crucial in transitioning between numerical simulation and actual orbital flight. Thus, the Advanced Autonomous Multiple Spacecraft (ADAMUS) laboratory at the University of Florida has designed a 3DOF experimental test-bed for hardware-in-the-loop validation of GN&C algorithms for formation flying reconfiguration (see Figure 10).

The experimental facility consists of two completely autonomous vehicles floating on an epoxy 4×4 m surface. The vehicles are equipped with eight compressed air thrusters to enable their movement (i.e. translational and attitude control) on the frictionless floor. The thrusters consist of solenoid valves attached to custom made nozzles, which are commanded by a relay module. All on-board subsystems of the floating vehicle are powered by a Lithium-Ion battery. The battery is connected to a Power Management System from Ocean Server Technology, namely the Intelligent Battery and Power System (IBPS). It recharges the batteries using a safety charging circuit when connected to the 120V grid and provides the required power at 5-12-24V voltages. Specifically, the IBPS provides 5V power to the onboard computer and 12V power to a secondary DC-DC converter, which brings the voltage to 24V to supply the thrusters' electro-valves.

An indoor navigation system, namely the PhaseSpace Impulse System, determines robots position and orientation on the frictionless floor. It consists of three main components: i) an array of 12

cameras situated around the test-bed, ii) 6 LEDs placed in key locations on the vehicles for determining the attitude and position of the vehicle, and iii) a dedicated computer for the position and attitude (quaternion) computation. The cameras capture the images of the flashing LEDs and the PhaseSpace computer determines the position of each LED according to its flashing frequency (specific to each LED). Ultimately, the vehicles are equipped with the Intrepid computer board equipped with a AT91SAM92G0 Processor @400 MHz (see Figure 11).

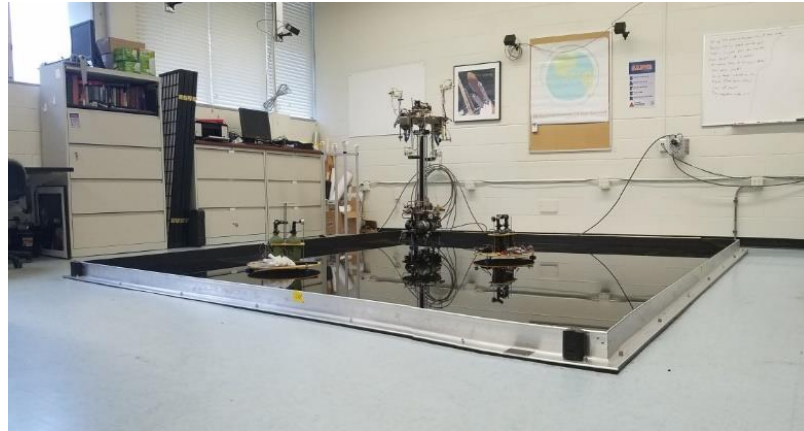


**Figure 10. ADAMUS testbed**

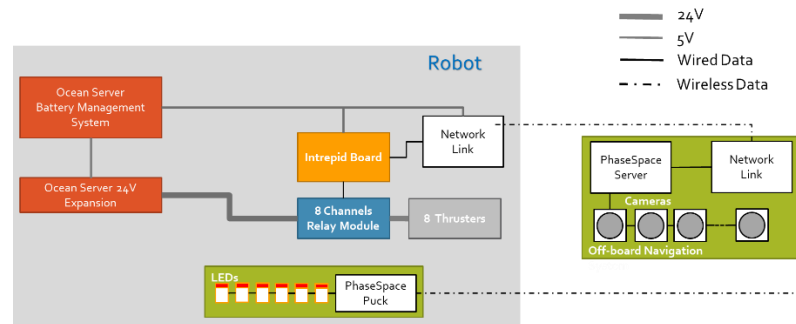


**Figure 11. Electrical and data architecture of testbed**

To emulate the orbital dynamics of the deputy satellite relative to the Radial-Tangential-Normal (RTN) reference frame centered at the chief, the inertia acceleration/torque and the gravitational force/torque, besides the control signal, have been computed onboard and reproduced by thrusters system. All orbital perturbing/control accelerations simulated by the vehicle have been scaled to satisfy the facility constraints. A linear quadratic regulator has been designed to compute the control signal, whereas the reference trajectory to be tracked has been generated onboard using the T-T-T analytical ROE-based control solution (see section 3.4.2.2). Finally, pulse-width pulse-

frequency (PWPF) modulator is used to translate continuous control commands given by LQR to on-off signals to thrusters.

## 4.0 RESULTS AND DISCUSSION

### 4.1 SURVEYS

#### 4.1.1 Dynamics Models

The work conducted under this grant provided a first-of-a-kind quantitative comparison between a wide range of dynamics models derived using various assumptions and state representations [1]. A key finding from this work is that linear dynamics models based on relative orbital elements provide the best propagation accuracy of all linear models in literature in a wide range of orbit scenarios. A comparison of the propagation accuracies of considered models in an orbit with an eccentricity of 0.5 and perigee altitude of 750 km is shown in Figure 12. A noteworthy feature of this plot is that the linear models developed in this work (indicated by KGD) outperform all other models except for the fully nonlinear Yan-Alfriend model.

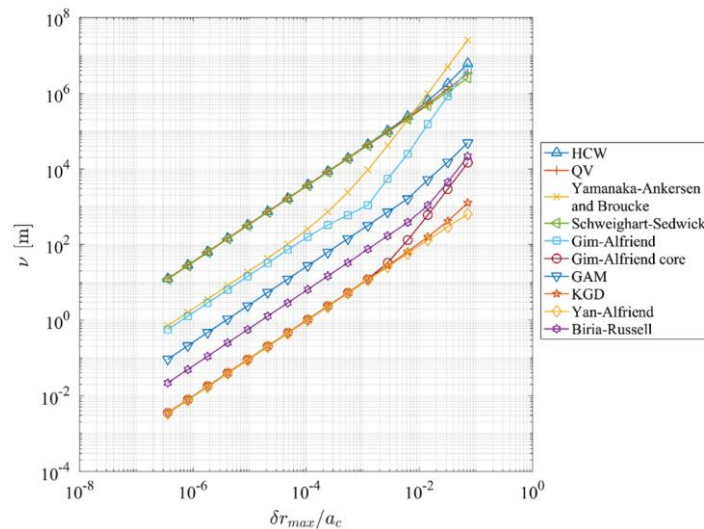


**Fig. 12: Propagation accuracy of relative motion models in literature compared to numerically integrated ground truth including J<sub>2</sub>-J<sub>5</sub>**

#### 4.1.2 GN&C Requirements

Based on the survey carried out about on onboard GN&C subsystem [2], the requirements for control and navigation functions have been identified. As illustrated in Table 5, space science missions tend to be the most demanding in terms of relative orbit control accuracy. These missions include, among others, space-based telescopes such as the X-ray Evolving Universe Spectroscopy

(XEUS) mission, a dual spacecraft x-ray telescope operating in a low perturbed environment (e.g., LPO) and designed by the ESA in collaboration with NASA to investigate the high-redshift universe. For this type of mission, high accuracy (order of millimeters to centimeters) is due to the alignment requirements for the observatory elements, the mirror, and the detector. A lower accuracy is generally needed by Earth observation/remote sensing and Earth science missions (hundreds of meters and kilometers, respectively). Two examples of these categories are TanDEM-X and GRACE. TanDEM-X requires a control accuracy of 20 *m* in the radial and normal direction and 200 *m* along-track, whereas the two spacecraft of GRACE have to maintain a relative along-track distance of  $200 \pm 50$  *km* during the nominal science operations. It is worth remarking that that achieving the performances reported in Table 5 might pose different challenges from a control design standpoint, depending on the operating orbital regime. In other words, meeting high control accuracy in low Earth orbit (e.g., centimeter level) might be much more challenging than meeting the same requirement at the Lagrange point due to the different values of differential perturbing accelerations acting on the spacecraft.

**Table 5. Relative orbit control accuracy and mean inter-satellite distance for objective-related class of formation flying missions**

<i>Formation Flying Mission classes</i>	<i>Accuracy Range</i>	<i>Inter-satellite distance</i>
Space science	0.1 – 10 cm	35 m – 80,000 km
Earth science	100 m – 50 km	50 – 200 km
Earth observation/remote sensing	10 – 200 m	50 m – 100 km

Table 6 summarizes the navigation accuracy for each objective-related class of missions. Accordingly, the most demanding requirements are associated with space science missions. The low corresponding accuracy value reported in Table 6 relies on the deep space dual-spacecraft telescope planned to fly in the future, as EXO-S or Stellar Imager. Future distributed systems for the deep-space observation, in fact, will require a high control performance to achieve their mission goals and, consequently, a navigation system that enables us to estimate the relative state with extraordinary precision. Earth science and Earth observation missions show less strict constraints on the navigation accuracy, varying from 1 to 10 m. This fact is due to the lower accuracy for these missions on the required control performances.

**Table 6. Relative navigation accuracy for objective-related class of FF missions**

<i>Formation Flying Mission classes</i>	<i>Accuracy Range</i>
Space science	1 mm – 100 m
Earth science	1 – 10 m
Earth observation/remote sensing	1 – 10 m

Ultimately, from the presented survey three key aspects emerged: future missions will 1) require more onboard autonomy, 2) higher dynamic range performance, and 3) exploit a smaller satellite bus to accomplish their goals. These technological trends pose new challenges for the design of the GN&C system, mainly related to the development of robust and accurate methodologies for the orbit control and relative navigation, as well as computationally efficient techniques for the guidance. In light of this, new relative dynamics models that allow the inclusion of orbital perturbations, such as solar radiation pressure and third body from (at least) the sun and moon, and the determination of associated analytical solutions to improve the performance of the guidance and filtering process should be investigated. In addition, efficient orbit control techniques capable of combining the continuous-thrust and impulse solutions for spacecraft maneuvering in order to satisfy the low-thrust constraints and to meet the robustness/flexibility requirements due to the growing onboard autonomy should be developed.

## 4.2 DYNAMICS

### 4.2.1 Linear Dynamics Models

[3] [4] [5] expand over the state-of-the-art by developing new linear dynamics models which fulfill orbit propagation accuracy requirements needed by on-board GN&C algorithms in a multitude of orbit scenario. In [3], the J2+drag state transition matrices are derived using two types differential drag models: 1) a density model-specific formulation that requires a priori knowledge of the atmosphere, and 2) a density-model-free formulation that requires inflight estimation of time derivatives of specified state components. These models are used to provide a simple geometric interpretation of the effects of these perturbations on spacecraft relative motion (Fig. 13) and harmonize current literature on state transition matrices. The models are validated by comparing open-loop propagation of three test cases with a high-fidelity numerical orbit propagator. These test cases include formations in near-circular, moderately eccentric, and highly eccentric orbits with inter-spacecraft separations of a few hundred meters, a few kilometers, and tens of kilometers, respectively. The density-model-free state transition matrices were found to be much more accurate than their density-model-specific counterpart. Indeed, the density-model-free state

transition matrices for orbits of arbitrary eccentricity are able to match or exceed the propagation accuracy of models available in the literature in all tested scenarios (Fig. 14), more details can be found in [3].

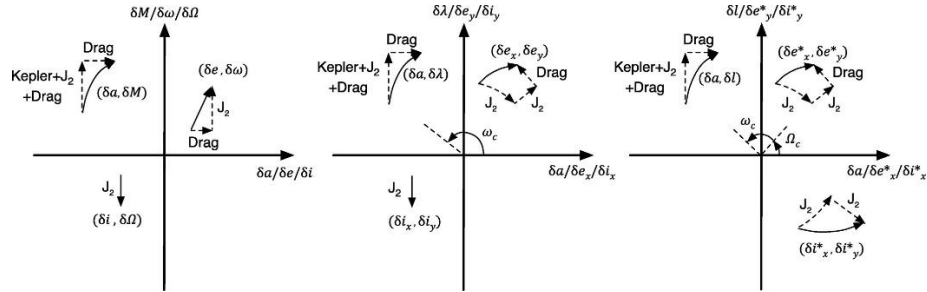


**Figure 13. Combined effects of Keplerian relative motion, J2, and differential drag on ROEs in eccentric orbits**

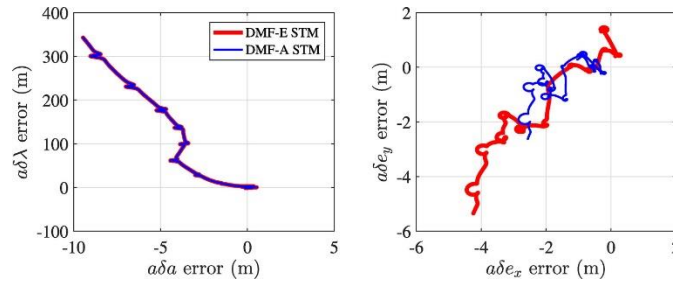


**Figure 14. Evolution of the in-plane density-model-free STM propagation errors for highly eccentric orbit test with a Jacchia–Gill atmosphere**

In [5], the J2+SRP state transition matrices are derived using: 1) an analytical model of SRP valid around an arbitrary celestial body in eccentric orbit around the Sun, 2) a model-free SRP formulation that require inflight estimation of time derivatives of specified state components. The analytical model is used to provide simple geometric interpretation of the effects of SRP on the spacecraft relative motion (Fig. 15). The models are validated by comparing open-loop propagation of three test cases with a high-fidelity numerical orbit propagator. These test cases include formations in near-circular geostationary orbit (GEO), high eccentricity geostationary transfer orbit (GTO), and high-altitude orbit around near-Earth asteroid Eros in eccentric orbit around the sun. The new J2+SRP state transition matrices have accuracy in the range of meters to few tens of meters in all orbit scenarios considered (Fig. 16), more details can be found in [5].



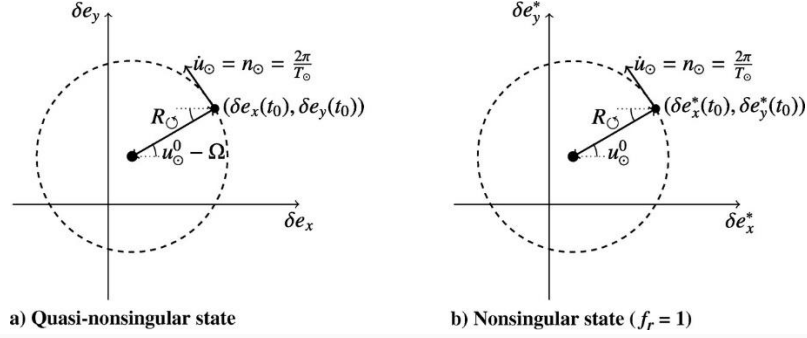


**Figure 15. Relative eccentricity vector circulation in near-circular Earth equatorial orbit due to SRP (eclipses neglected)**

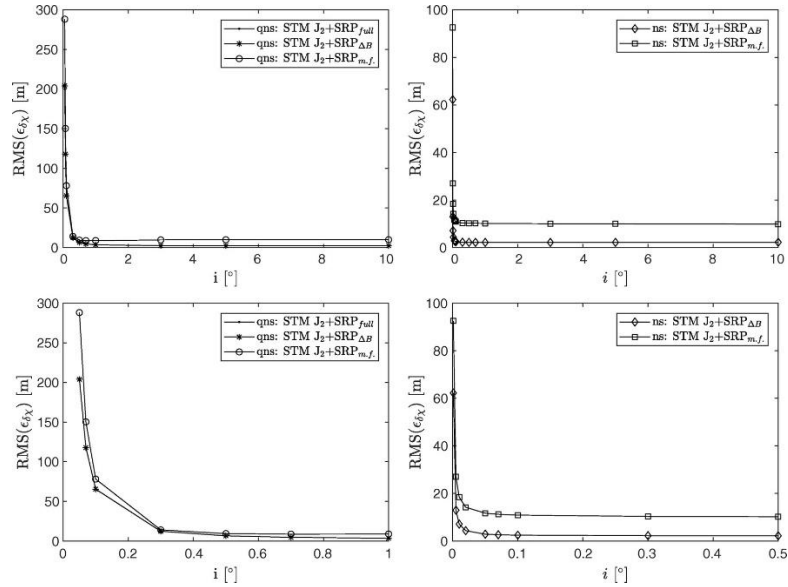


**Figure 16. Monte Carlo analysis varying the nominal chief orbit inclination of the formation in geostationary orbit: quasi-nonsingular state (left) and nonsingular state (right). Detailed views of the top plots are presented in the bottom plots**

#### 4.2.2 Second Order Dynamics Models

A performance comparison was performed between the new second-order solution for relative position and velocity on eccentric orbits and several prominent translational-state solutions [6]. Figure 17 shows the maximum position error over 10 orbits with respect to a Keplerian propagation for a range of orbit eccentricities. All scenarios are initialized at perigee with an altitude of 750 km and involve both in- and out-of-plane motion centered on the chief spacecraft. Dashed lines represent linear models, dash-dot are second-order, and dotted lines are third-order. Models with blue lines assume near-circular orbits and red fully incorporate eccentricity into the dynamics. The new second-order solution is more accurate than all related translational state models by several orders of magnitude for a wide range of orbit eccentricities. However, similar levels of accuracy may be obtained using very simple ROE models, and more sophisticated models that include

important perturbation effects were discussed in the previous section. There is a tradeoff in computational cost between the simplicity of a dynamics model and the state transformations needed to convert from observable quantities. For some applications it may be justifiable to use a second-order translational state solution over an orbital element-based model, however the increased complexity of third- and higher-order solutions makes them impractical.

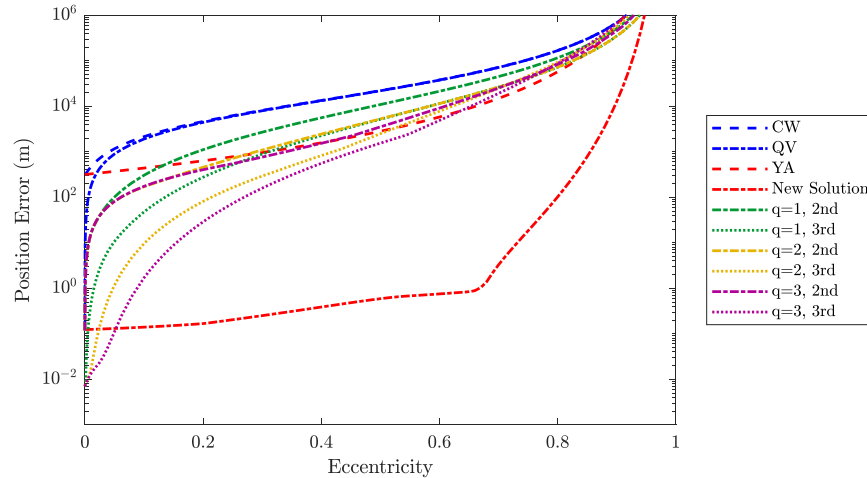


**Fig. 17: Maximum position error over 10 orbits using a range of eccentricities for a selection of translational state solutions compared to a Keplerian truth**

## 4.3 GUIDANCE

### 4.3.1 Swarming

The first two swarm geometries that ensure minimum separation between spacecraft and passively bounded relative motion in a  $J_2$ -perturbed near-circular orbit were developed in ROE space [7]. One formation geometry, called the E-I vector swarm design, is an extension of the binary E-I vector separation formation design, and the second formation geometry, called the high density swarm design, is an in-plane swarm that achieves the highest satellite density while ensuring a minimum separation between the spacecraft.

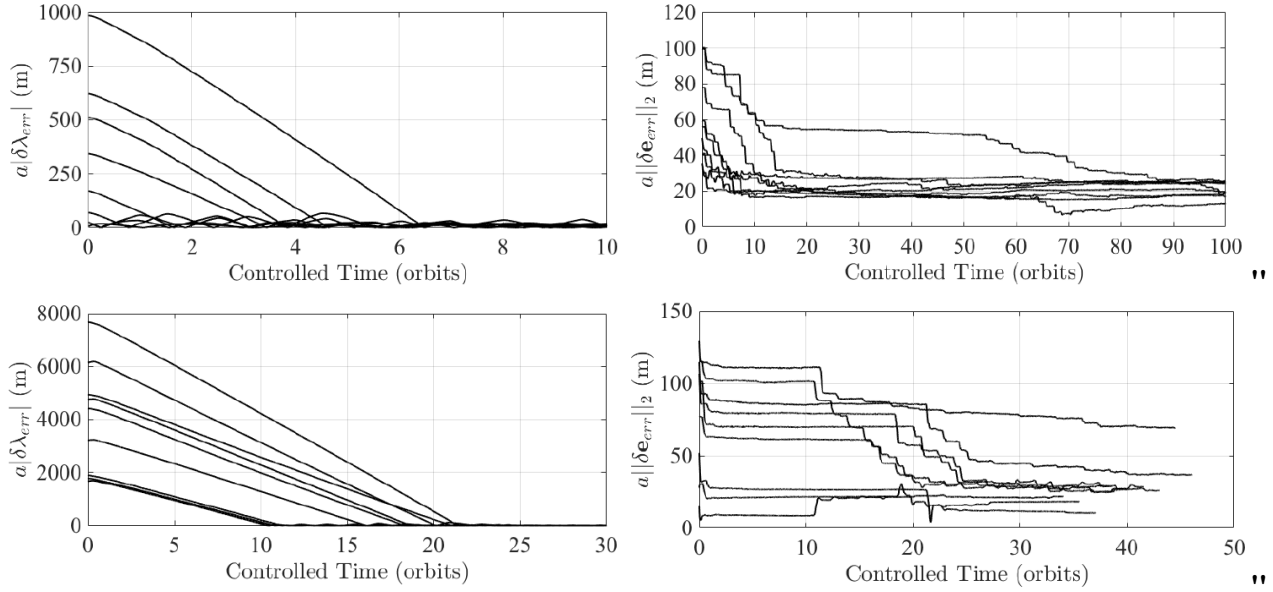
Two formation-keeping approaches were designed to maintain the designed swarm geometries: low-thrust and drag control. The low-thrust control algorithm leverages ROE to design a computationally efficient state-space control algorithm that maintains formation geometry and guarantees safety. The drag control algorithm leverages the known low earth orbit environment to produce a formation keeping algorithm that relies on natural dynamics to avoid fuel consumption. The results of the control algorithm implementation for a swarm in a near-equatorial, near-circular orbit with a 450 km altitude simulated for 10 weeks is provided in Table 7, where the left column represents the E-I separation swarm design and the right column represents the high density swarm design. Both swarms demonstrate a minimum separation ( $\delta r$ )

greater than the guaranteed 100 m and fuel usage for the swarm on the order of cm/s. Additionally, the largest ROE parameters and error in the relative eccentricity vector is provided. Finally, note that  $P_{\max}$  and  $P_{\text{mean}}$  denote maximum largest and mean torque produced from the reaction wheels recorded on any deputy spacecraft for the drag control scenario.

**Table 7. Results of the control algorithm implementation for a swarm in a near-equatorial, near-circular orbit with a 450 km altitude simulated for 10 weeks**

<i>Parameter</i>	<i>Unit</i>	<i>Value</i>	<i>Parameter</i>	<i>Unit</i>	<i>Value</i>
Low-thrust control			Low-thrust control		
$\min(\delta r)$	m	211	$\min(\delta r)$	m	158
$\Delta v$	cm/s	64	$\Delta v$	cm/s	19
$\max(a \delta a )$	m	36	$\max(a \delta a )$	m	4.6
$\max(a \delta \lambda )$	km	7.7	$\max(a \delta \lambda )$	km	29
$\max(a\ \delta \mathbf{e}_{\text{err}}\ _2)$	m	105	$\max(a\ \delta \mathbf{e}_{\text{err}}\ _2)$	m	29
Drag Control			Drag Control		
$\min(\delta r)$	m	280	$\min(\delta r)$	m	187
$P_{\max}$	$\mu\text{N/m}$	24	$P_{\max}$	$\mu\text{N/m}$	24
$P_{\text{mean}}$	$\mu\text{N/m}$	0.82	$P_{\text{mean}}$	$\mu\text{N/m}$	0.65
$\max(a \delta a )$	m	17	$\max(a \delta a )$	m	1.6
$\max(a \delta \lambda )$	km	2.8	$\max(a \delta \lambda )$	km	29
$\max(a\ \delta \mathbf{e}_{\text{err}}\ _2)$	m	50	$\max(a\ \delta \mathbf{e}_{\text{err}}\ _2)$	m	23

The deployment of the two specified swarm geometries was addressed with uncertainties in [8]. The deployment approach leverages uncertainties in a representative cube-sat launcher to analytically determine the commissioning windows, where spacecraft do not have actuating ability, for the deputies. The deployment approach guarantees minimum separation for safety but also ensures a maximum separation to enable communication between satellites. The results in Figure 18 indicate the error in ROE space of each deputy satellites over time, where the error is defined as the difference between the current and the goal ROE to attain the desired swarm formation. The top subfigure pertains to the high-density swarm design, and the bottom subfigure pertains to the E-I vector separation design.



Hli wtg'3: 0Vj g'gttqt 'lp'TQG'ir'ceg'qhgcej 'f grw{ 'lc'vgnksgu'qxtg 'llo g.'y j gtg'vj g'gttqt 'ku'  
f ghpgf 'cu'vj g'f Hlgt gpeg'dgyw ggp'vj g'ewt tgpv'cpf 'vj g'l qcnTQG'vq'cwclp'vj g'f gukt gf "  
uy cto 'hqt o cvkqp0'Vj g'vqr 'cpf 'dlqwqo 'lwdlhi wtgu'r'gt vclp'vq'vj g'j li j /f gpuk{ 'cpf 'G/K  
xgevqt 'lgr ct cvkqp'ly cto 'bes wklkqp.'t gur gevksgr{ "

6050' Kpvgi tcvkqp'Eqpucpwi'cu'Ucvg'Xct lcdigu'

[9] shows how a state parameterization based on integration constants (IC) introduces a simplification in the optimal path planning of multi-dimensional systems governed by ODE:

$$\begin{aligned} \min_u J &= \sum_{i=1}^N \|\Delta \mathbf{u}(t_i)\| \\ \text{subject to } \dot{\mathbf{c}} &= \frac{\partial \mathbf{c}}{\partial \boldsymbol{\chi}}(t) \mathbf{F}_p(t, \mathbf{c}) + \sum_{i=1}^N \boldsymbol{\Gamma}(t_i) \Delta \mathbf{u}(t_i) \\ \mathbf{c}(t_0) &= \mathbf{c}_0 \quad \mathbf{c}(t_f) = \mathbf{c}_{goal} \end{aligned} \quad (2)$$

$$\begin{aligned} \min_u J &= \sum_{i=1}^N \|\Delta \mathbf{u}(t_i)\| \\ \text{subject to } \dot{\boldsymbol{\chi}} &= \mathbf{F}'(t, \boldsymbol{\chi}) + \mathbf{F}_p(t, \boldsymbol{\chi}) + \sum_{i=1}^N \mathbf{B}(t_i) \Delta \mathbf{u}(t_i) \\ \boldsymbol{\chi}(t_0) &= \boldsymbol{\chi}_0 \quad \boldsymbol{\chi}(t_f) = \boldsymbol{\chi}_{goal} \end{aligned} \quad (3)$$

where Eq. 2 represents the formalization in IC space, whereas Eq. 3 in cartesian operative space. In particular, the solution of the optimal control problem in IC space leverages intrinsically the

integrable part of the dynamics, while the perturbative part is isolated and then fully, or at least partially, compensated. This opens the way to a direct geometrical interpretation and possible geometrical resolution of the optimal path planning problem (Figure 19).

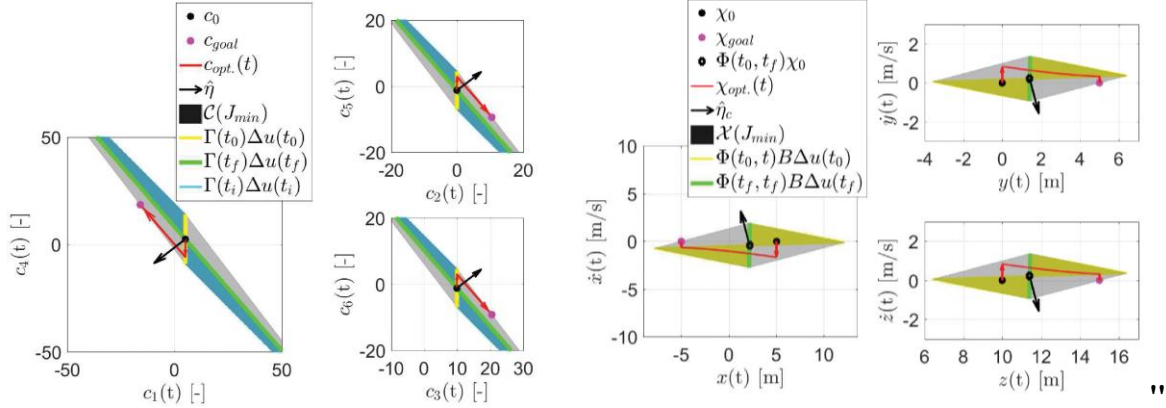


Figure 19: Optimal path planning problem. The figure consists of six subplots. The top row shows the cost function  $J(t)$  vs time  $t$ , with  $J(t)$  decreasing from  $J(0)$  to  $J(t_f)$ . The middle row shows the optimal path  $X_{opt}(t)$  in the  $x-y$  plane, with the path starting at  $X(0)$  and ending at  $X(t_f)$ . The bottom row shows the optimal path  $X_{opt}(t)$  in the  $x-z$  plane, with the path starting at  $X(0)$  and ending at  $X(t_f)$ .

### 6.5.1. Input-shaping based analytical guidance solution

Two different scenarios are considered to assess the effectiveness of proposed input-shaping based analytical guidance solution. In the first one (Case 1) the deputy has no relative radial displacement and velocity. For the second scenario (Case 2) the initial condition is assumed to be an equilibrium motion, i.e.,  $\dot{y}_0 = -2\bar{m}x_0$  (see Table 8). Without loss of generality, maximum thrust magnitude is assumed  $\bar{u} = 2 \cdot 10^{-8} \text{ km/s}^2$  and the desired along-track location of the center of the final relative ellipse is  $\bar{y}_d = 0$ .

Table 8: Initial conditions for the input-shaping based analytical guidance solution

Legend	$x_0$ [m]	$y_0$ [m]	$\dot{x}_0$ [m/s]	$\dot{y}_0$ [m/s]
Case 1	0	-4.258	0	0
Case 2	-0.604	-4.258	0.0004	0.0014

For the sake of brevity, only the trajectory obtained using the ZVD shaper with  $\Delta t/T = 0.5$  for Case 2 is illustrated. Initial relative state has been propagated through a nonlinear dynamics model including the perturbing effects of  $J_2$ . As showed in Figure 20, at the end of the maneuver (i.e.,  $t_m = t^* + 2\Delta t$ ), the position error,  $e_{pos} = \sqrt{x(t_m)^2 + y(t_m)^2}$ , between the guidance and the nonlinear trajectory is 107 m. In addition, the center of the relative ellipse is shifted of 186 m with respect to the desired position (i.e.,  $\bar{y}_d = \bar{x}_d = 0$ ). It is worth remarking that the inclusion of  $J_2$  through the SS dynamics model for the shaper design has allowed improving the accuracy of the

guidance solution. In fact, in past study it has been shown that the guidance solution given by the ZVD shaper based on the unperturbed dynamics model provides an accuracy of 445 m.

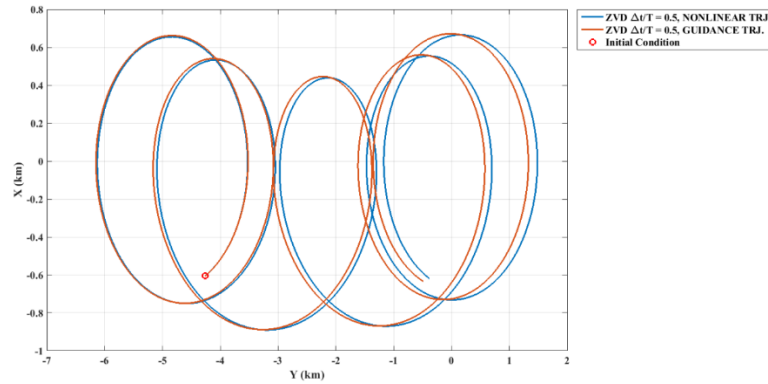


Figure 20: Trajectory corresponding to optimized ZVD-based solution for Case 2, assuming a desired value for the final relative eccentricity of 0.7. The optimizer initial guess (i.e.  $\Delta t/T = 0.5$ ,  $\alpha = 0^\circ$ ) gives a final relative eccentricity equal to the initial one, i.e.  $e_{rel,f} = 0.67895$ , with a maneuvering cost of a  $\Delta V = 0.305$  m/s. On the contrary the optimized solution leads to a higher delta-v,  $\Delta V = 0.334$  m/s. However, it guarantees the achievement to the desired formation configuration.

Ultimately, Figure 21 shows the trajectory corresponding to optimized ZVD-based solution for Case 2, assuming a desired value for the final relative eccentricity of 0.7. The optimizer initial guess (i.e.  $\Delta t/T = 0.5$ ,  $\alpha = 0^\circ$ ) gives a final relative eccentricity equal to the initial one, i.e.  $e_{rel,f} = 0.67895$ , with a maneuvering cost of a  $\Delta V = 0.305$  m/s. On the contrary the optimized solution leads to a higher delta-v,  $\Delta V = 0.334$  m/s. However, it guarantees the achievement to the desired formation configuration.

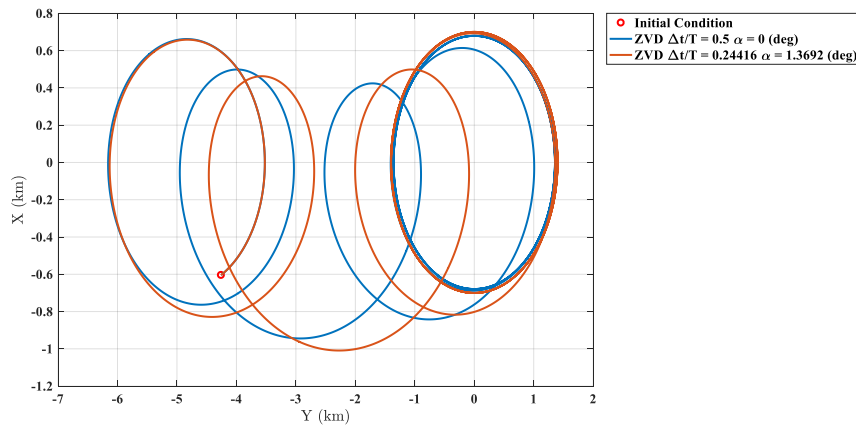


Figure 21: Trajectory corresponding to optimized ZVD-based solution for Case 2, assuming a desired value for the final relative eccentricity of 0.7. The optimizer initial guess (i.e.  $\Delta t/T = 0.5$ ,  $\alpha = 0^\circ$ ) gives a final relative eccentricity equal to the initial one, i.e.  $e_{rel,f} = 0.67895$ , with a maneuvering cost of a  $\Delta V = 0.305$  m/s. On the contrary the optimized solution leads to a higher delta-v,  $\Delta V = 0.334$  m/s. However, it guarantees the achievement to the desired formation configuration.

606' EQPVTQN"

"

606B' Kō rwnkxg'Eqpvt qnl'

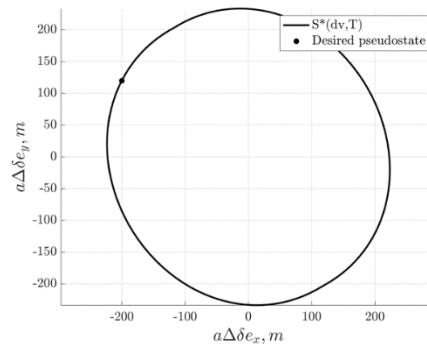
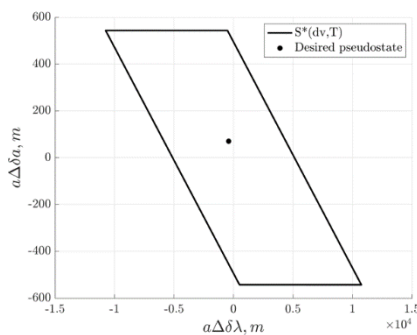
"

606B8'Emugf /hqt o 'Uqmwkqpu'Cr rt qcej "

This section will demonstrate the application of the general methodology in Section 3.4.1.1 to the quasi-nonsingular ROE state for a reconfiguration with an eccentric chief orbit. The resulting closed-form expressions can be found in [12]. The reconfiguration parameters for this example are given by

$$\begin{aligned}\alpha_{c,0} &= [16600 \text{ km}, 0.6, 20^\circ, 0^\circ, 30^\circ, 0^\circ] \\ a\delta\alpha_0 &= [30, -10500, 0, -50] \text{ m} \\ a\delta\alpha_f &= [100, -12500, -200, 70] \text{ m} \\ t_f &= 2.1 \text{ orbits}\end{aligned}\tag{4}$$

where  $\alpha_{c,0}$  are the absolute orbital elements of the chief,  $a\delta\alpha_0$  are the initial relative orbit elements,  $a\delta\alpha_f$  is the final desired relative orbit elements, and  $t_f$  is the reconfiguration time. The general methodology to derive the reachable minimum delta-v yields a cost of  $\delta v_{min} = 40.06 \frac{mm}{s}$  required to achieve the example reconfiguration. Figure 22 shows the reachable set,  $S^*(c, T)$ , plotted for  $c = \delta v_{min}$ . In the relative eccentricity vector plane, the desired end state lies on the boundary, so  $40.06 \frac{mm}{s}$  is the optimal delta-v. "

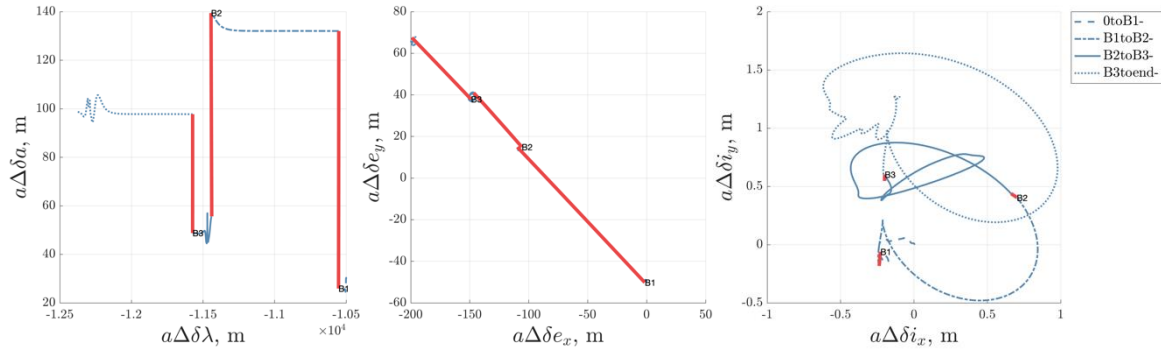


Hli wt g'44<Tgcej cdrg'lgw'lp'vj g'r t qlgevfg 't g0b gcp'iqpi kwf g.'t g0lgo kō clqt 't zku'iglw' cpf 't gr vkg'geegpvt kls{ 'xgevqt '\*t li j v+ 'r npgu0Vj g'f gult gf 'gpf 'lncvg'lguf k gev{ 'qp'vj g' dqwpf ct { 'qh'vj g'eqpxgz'j wnilp'vj g't gr vkg'geegpvt kls{ 'xgevqt 'r npg'\*t li j v+ 'uq'62'b o 'lu'ku' vj g'qr vko cuf gnc/x'ēpf 'vj g't geqplhi wt cvkp'ku'f qo hpcpv'lp't gr vkg'geegpvt kls{ 'xgevqt "

"

Once the reachable  $\delta v_{min}$  is computed, the reachability of the full 6D reconfiguration can be assessed. For this example, the desired end state lies inside the reachable set formed by mapping the optimal times and maneuvers from the dominant plane onto the non-dominant planes (not

shown), so a maneuver scheme that achieves the full desired reconfiguration with cost equal to the optimal delta-v can be found, as shown in Figure 23.



Hi wt g'45<'Gxqmwkp'qh'vj g'TQG'kp'vj g'4F'rtqlgevgf'rtcpgr'tqr ci cvgf'y kj 'b cpgwxgt u'  
wpf gt'hmw/hqteg'f { pco ku'b qf gr'

Even though maneuvers were planned excluding all external perturbations, when propagated in a full-force dynamics simulation, the error between the desired value and the achieved value of ROE was 1.27%, 0.91%, 1.17%, 8.01% for  $a\delta a$ ,  $a\delta\lambda$ ,  $a\delta e_x$ ,  $a\delta e_y$  respectively.

60604 Pwo gtkecdCni qtkj o "

The developed algorithm provides globally optimal solutions to a challenging class of energy-optimal impulsive control problems with greater robustness and less computation cost than comparable approaches in literature. In conducted tests, the algorithm was able to solve 1000 different optimal control problems in eight or fewer iterations of the refinement algorithm. A Monte Carlo experiment was conducted for example formation reconfiguration problems and it was found that the algorithm's computation cost is insensitive to poor initializations. The number of iterations of the refinement algorithm required to converge to a solution with a cost within one percent of the global optimum for 1000 example problems is shown in Fig. 24 for three different initialization schemes. It is evident that the worst-case initialization (including only two times), requires only one additional iteration on average.



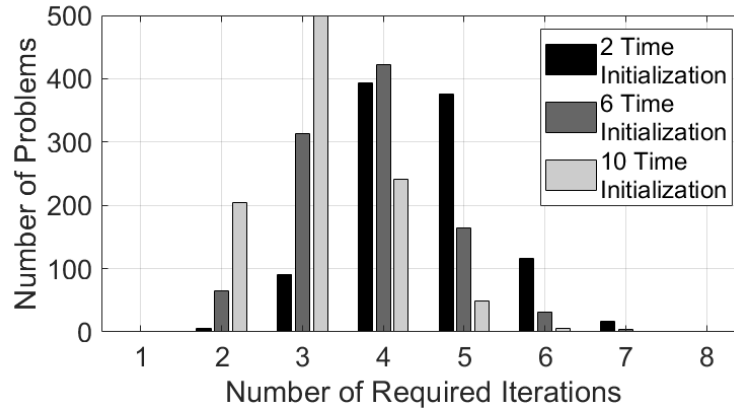


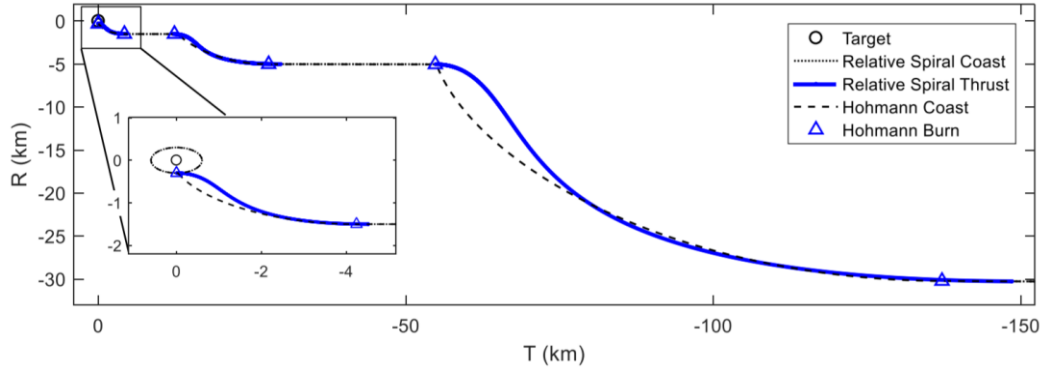
**Fig. 24: Required refinement iterations for convergence to a solution with a cost within one percent of the global optimum for 1000 example problems**

Also, the runtime for the proposed algorithm was found to be nearly constant (2-5 seconds on a desktop computer) for up to 10000 samples of the time domain. This is more than 25 times faster than comparable state-of-the-art algorithms in literature.

## 4.4.2 Continuous Control

### 4.4.2.1 Spirals Approach

The relative spiral trajectory design method was tested in several formation acquisition and reconfiguration scenarios. Figure 25 compares the trajectories in the radial-transverse-normal frame of the target spacecraft for a formation acquisition scenario using impulsive Hohmann transfers and continuous-thrust relative spirals [14]. In this scenario the deputy spacecraft begins at a large distance behind the target, harnessing Keplerian drift to approach it steadily on lower-altitude holding orbits. Although the Hohmann transfers achieve minimum delta-v, they require instantaneous velocity changes, indicated by the sharp corners on the dashed trajectory. The relative spiral approach incurs a delta-v penalty due to kinematic inefficiency, but achieves the target orbit with continuous low-thrust maneuvers. When the higher specific impulse of low-thrust propulsion systems is taken into account, the propellant cost of the relative spiral trajectory is much lower than that required for Hohmann transfers.



Hi 047<Eqo rctkqp'qhlqto cvkqp'ces wklkqp't clgevqt lgu'wulpi 't grvkg'ur kt cn'y kj ''  
eqpvpwqwu/vj twu'cpf 'J qj o cpp't cpulgtu'y kj 'lo rwnkg'b cpgwxgtu'

60604 TQG'Crrtqcej ''

The performance of proposed control strategies in terms of maneuvering cost and accuracy has been validated though the simulation setup illustrated in Figure 26. First, the initial mean orbit elements of the chief and the mean ROE state are set. Then, the initial mean orbit elements of the deputy are computed. A numerical propagator including the Earth's oblateness J2 effects is used to obtain the history of position and velocity of chief and deputy spacecraft expressed in the Earth Centered Inertial (ECI) reference frame (J2000). The initial Cartesian states of both satellites are derived using the linear mapping developed by Brouwer and Lyddane to transform the mean orbit elements into osculating and the nonlinear relations between Cartesian state and osculating elements. The control thrust profile is projected in ECI and added as external accelerations to the deputy's motion. After the simulation, the absolute position and velocity of the spacecraft are converted into the mean orbit elements to compute the accuracy at the end of the maneuver, defined as

$$\epsilon_{\Delta\alpha_r}(t) = \frac{\Delta\alpha_r^{num}(t) - \Delta\alpha_{r,des}}{|\Delta\alpha_{r,des}|} \quad r = 1, \dots, 6 \quad (5)$$

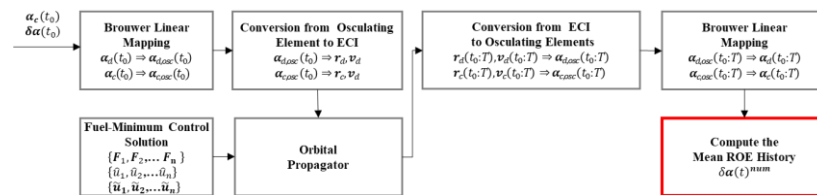
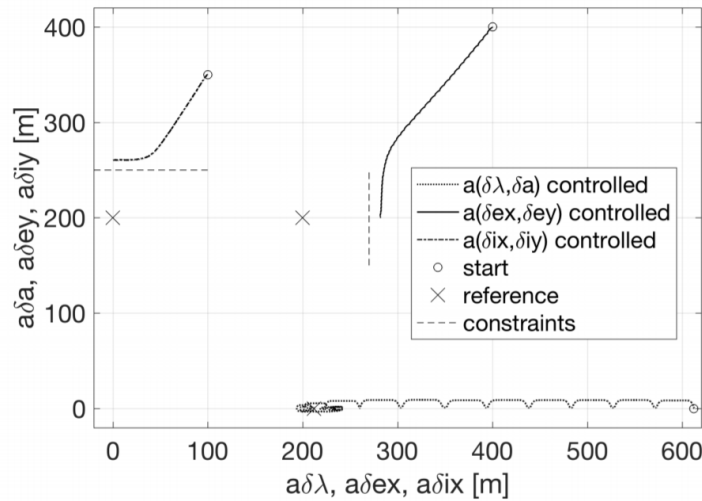


Figure 26. Simulation setup for the validation of proposed control strategies''

Numerical simulations have showed that the derived continuous solutions (analytical or numerical) for reconfiguration problem always guarantee a higher accuracy than the corresponding impulsive

solutions, reducing the relative position and velocity errors at the end of maneuvering interval, even though they require higher delta-V. In further details, it has turned out that continuous control solutions provide accuracy 2 orders of magnitude greater than the corresponding impulsive one [17][19]. Ultimately, it has been proven that the methodologies proposed for the design of fuel-minimum reconfiguration maneuver can achieve an accuracy of order of millimeter. In addition, the conducted analyses have demonstrated the computational efficiency of the MILP approach against the PSO one, [18]. However, for the sake of completeness, it must be pointed out that computational performances of MILP solver are affected by complexity of the problem, besides the number of optimization variables and inequalities constraints. For instance, when the collision avoidance and the additional time constraints have been included in the formulation, the MILP has found a feasible control solution in more than 2 min. On the contrary, if only the limitations on the control acceleration have been taken into account, the MILP approach has been able to provide the control scheme in less than 30 s, regardless the chosen time mesh size, [16].

Regarding [20], by defining a potential function with a minimum at the desired ROE state and maximums defined by circular and wall constraints, a particular spacecraft state can be guided to the goal state while avoiding prohibited ROE combinations. In order to achieve the goal state, the Reference Governor (RG) defines an allowable short-term goal that moves along the descent direction of the potential field. The short-term goal provided by the RG accounts for the wall and circular constraints as well as thrust and time constraints to ensure reconfigurations occur within desired time frames without exceeding thruster capabilities. A Lyapunov feedback controller uses this short-term goal by producing a Lyapunov function with a minimum corresponding to the goal state. The implemented feedback controller cancels the relevant dynamics in order to move directly towards the goal state. The feedback gain matrix used in the controller is composed of an in-plane and out-of-plane submatrix. The in-plane sub-matrix is adjusted throughout the orbit period to ensure that the implemented maneuver reduces state error in the relative eccentricity vector and relative semimajor axis simultaneously based on knowledge provided by the ROE representation. The in-plane and out-of-plane submatrix are designed to implement a continuous thrust maneuver with throttling up to a maximum acceleration and back down to zero to provide realistic thruster behavior. An example reconfiguration in a near-circular, retrograde low earth orbit is shown in Figure 27, where the goal ROE state  $a\delta\alpha = (0, 212, 200, 200, 0, 200)\text{m}$  and initial ROE states  $a\delta\alpha = (0, 712, 400, 400, 0, 350)\text{m}$  are represented by x's and open circles, respectively. Notice that the states move directly along the vector defined from the initial state to the goal state until a constraint is encountered.



**Figure 27. Example reconfiguration with wall constraints for a chief-deputy pair in a near-circular, retrograde low earth orbit. The state is initialized to values defined by the open circles. The destination state is represented by x. Notably, the state moves directly along the vector defined from the initial state to the goal state until a constraint is encountered. Once a constraint is encountered, the controller attempts to move to a destination as close to possible to the goal state without violating the wall constraint**

## 4.5 NAVIGATION

### 4.5.1 Angles-only Navigation

The batch relative orbit determination algorithm developed in this work provides for the first time the ability to accurately estimate the relative state of a resident space object using only bearing angle measurements. In conducted tests, the algorithm provides state estimates with a range estimate within 20% of the ground truth and estimates of other relative orbital elements (ROE) with errors of better than 10m per kilometer of separation. This accuracy is comparable to estimates provided by NORAD two-line elements and is sufficient to initialize a sequential filter. The behavior of the errors in the estimates of each of the ROE after each regularized least-squares iteration for a single test case are shown in Fig. 28.

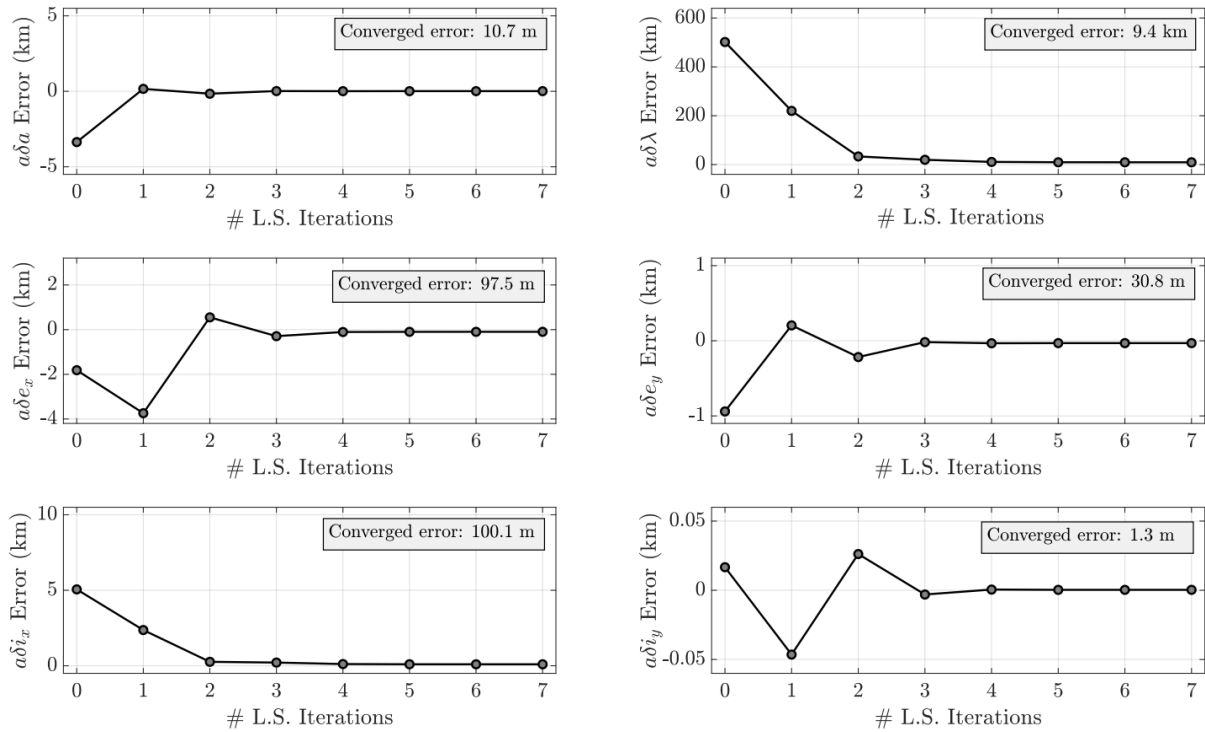


**Fig. 28: Evolution of estimation error for batch relative orbit determination after each regularized batch least squares iteration for example test scenario**

The developed sequential filter initialized with an estimate provided by the batch relative orbit determination algorithm was found to converge to a state estimate with a range error of less than 2% and errors in the other ROE of better than 1m per kilometer of separation in hardware-in-the-loop tests using the optical stimulator testbed [21-24]. This behavior was retained in test cases that include significant data outages (>30% of each orbit) due to eclipses and sparse measurement updates (2-5 minutes between images). Representative behaviors of the estimation error and formal covariance for the filter are shown in Fig. 29. The gray shaded regions indicate data outages due to eclipse. It is evident that the filter converges from the initial estimate in a few orbits and exhibits a steady-state range error of not more than a few hundred meters.

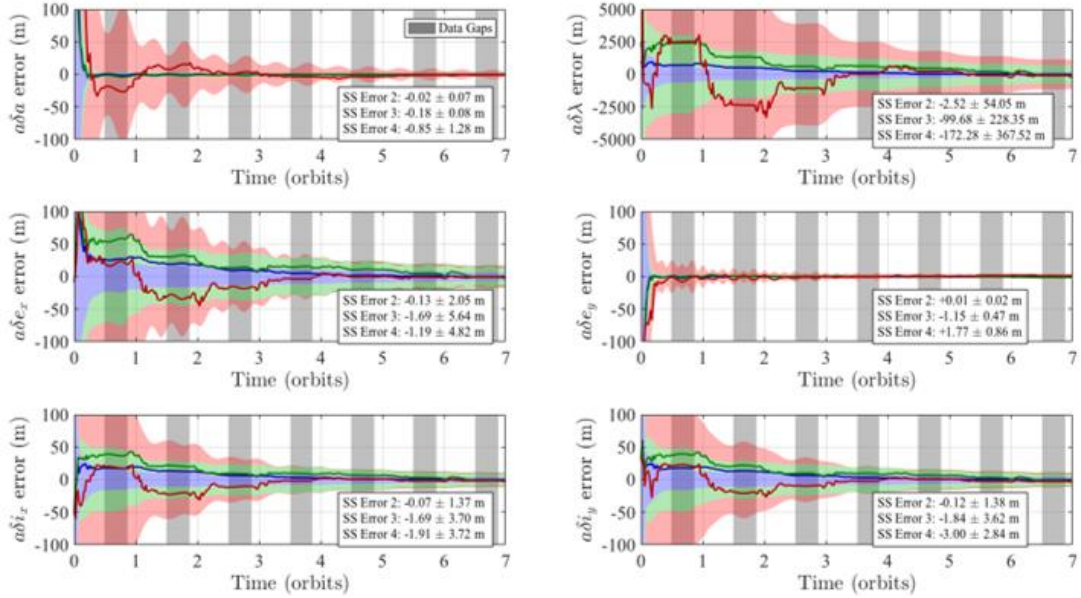


**Fig. 29: Evolution of state estimation errors (solid lines) and 3-sigma formal covariance (shaded regions) from numerical UKF using modeled measurements for three targets at different ranges including eclipses (gray bars)**

## 4.6 HIGH FIDELITY VALIDATION

### 4.6.1 Stanford's SLAB Virtual Reality Testbed

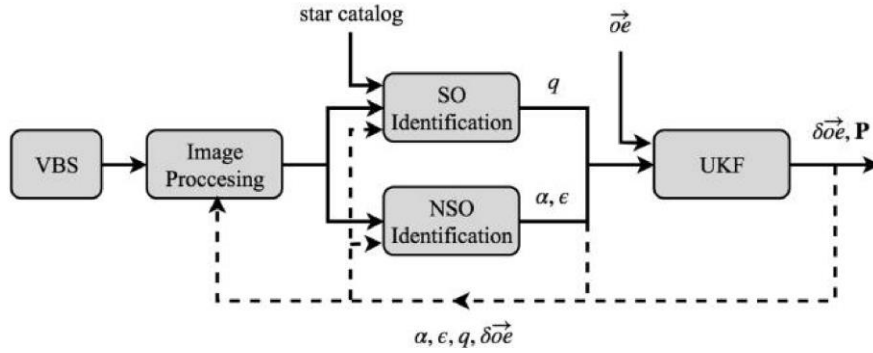
The SLAB's OS is used to perform hardware-in-the-loop validation of the Angles-Only Navigation Filter (see Section 4.5.1). Specifically, the problem of relative navigation of an observing spacecraft with respect to a non-stellar object (NSO) in a near-circular low Earth orbit (LEO) is considered. The initial observer mean orbital elements and mean ROE are reported in Tables 9 and 10, respectively.

**Table 9. Initial mean orbital elements of the observer**

$a_c$ (km)	$e$ (-)	$i$ (deg)	$\Omega$ (deg)	$\omega$ (deg)	$M_0$ (deg)
7200	0.001	30	60	120	0

**Table 10. Mean ROE for the test case**

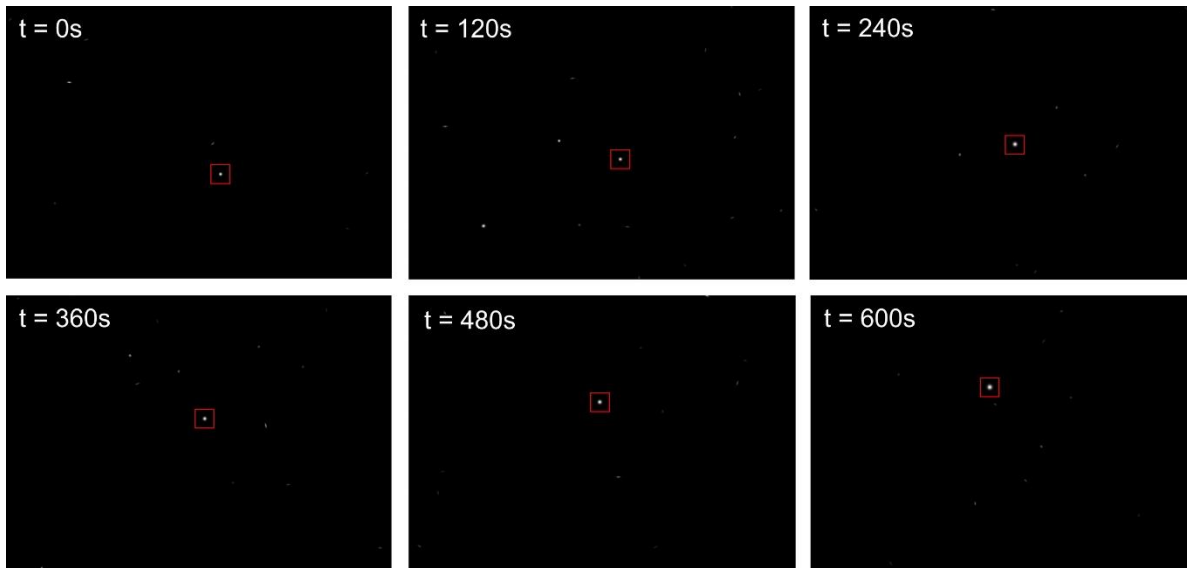
	$a_c \delta a$ (m)	$a_c \delta \lambda$ (m)	$a_c \delta e_x$ (m)	$a_c \delta e_y$ (m)	$a_c \delta i_x$ (m)	$a_c \delta i_y$ (m)
Initial ROE $\delta \alpha_0$	-50	-10,000	200	0	-200	0



**Figure 30. Architecture of hardware-in-the-loop AON algorithm**

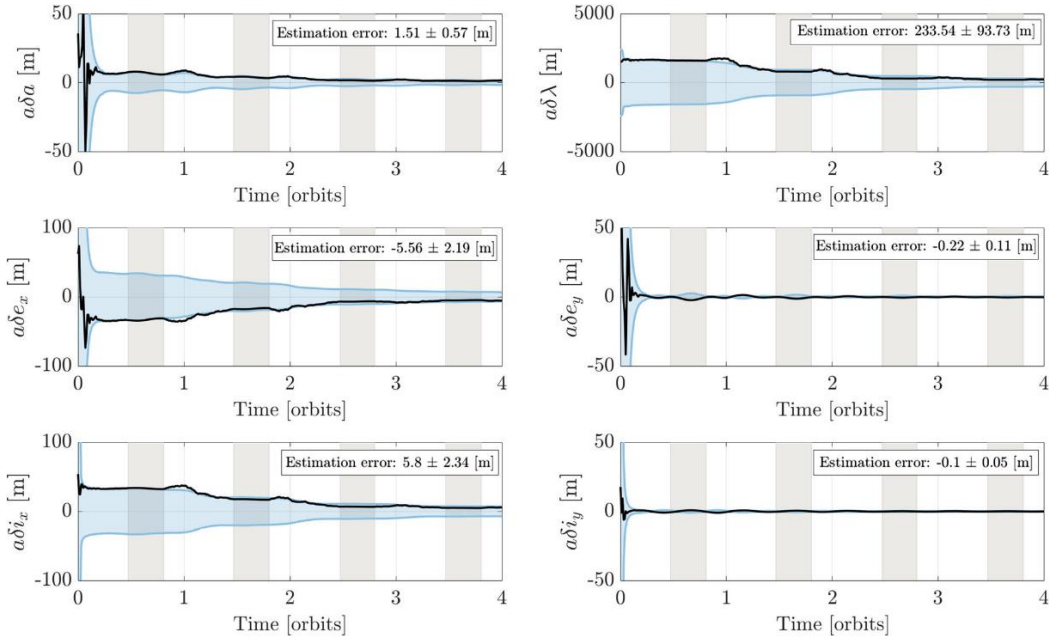
Figure 30 visualizes the simplified architecture of the AON algorithm with the OS in the loop. The image processing unit first identifies regions-of-interest from the images captured by the OS-stimulated VBS. Then, using a star catalog, the clusters of bright pixels are identified as either stellar objects (SOs) or NSOs, and the relevant subsystems provide estimates of initial attitude ( $q$ ) and bearing angle measurements ( $\alpha, \epsilon$ ), respectively. Given knowledge of the observer's current absolute orbital elements, the UKF provides the updated estimate of the ROE of the target with respect to the observer.

Figure 31 displays representative examples of OS images, as utilized in AON trials.



**Figure 31. OS images during AON trials. Both SOs and NSOs are present, with the target NSO outlined in red**

Figure 32 shows the performance of the UKF with OS in the loop. Steady-state estimation error of  $\alpha\delta\lambda$  is within 2.5% of the true mean inter-spacecraft range. Steady-state estimation error is within 10 m for all other ROEs.



**Figure 32. ROE estimation errors from the UKF. Vertical gray bars represent periods of eclipse**

#### 4.6.2 University of Florida's ADAMUS Lab Robotic Testbed

The performance of the T-T-T analytical ROE-based control solution (see section 3.4.2.2) has been validated at the University of Florida's ADAMUS Lab Robotic Testbed [28]. The control solution was applied to the initial and desired conditions provided in Table 11 and 12. The results of the implementation of the control solution on the ADAMUS testbed are shown in Figure 33 with the robot position referred to as "Robot" and the reference trajectory referred to as "Guidance". The error in the position and the reference trajectory for the X and Y-directions are shown in Figure 34.

**Table 11. Initial mean chief orbit in Keplerian orbital elements**

$a_c$ (km)	$e_{xc}$ (dim)	$e_{yc}$ (dim)	$i_c$ (deg)	$\Omega_c$ (deg)	$u_c$ (deg)
6578	0	0	8	0	0

**Table 12. Relative orbit at the initial and final maneuver time**

	$a_c \delta a$ (m)	$a_c \delta \lambda$ (m)	$a_c \delta e_x$ (m)	$a_c \delta e_y$ (m)	$a_c \delta i_x$ (m)	$a_c \delta i_y$ (m)
Initial relative orbit, $\delta \alpha_0$	0	2	0.5	0.5	0	0
Desired relative orbit, $\delta \alpha_{des}$	0	0	0.4	0.4	0	0



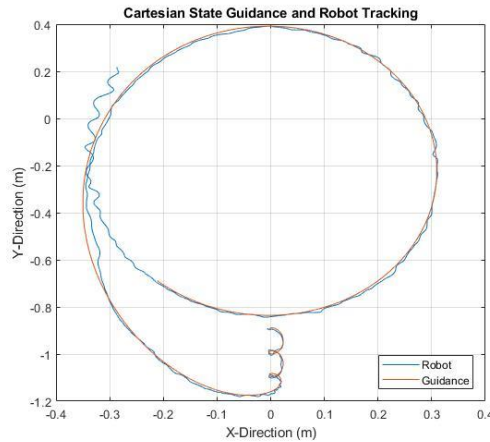


**Figure 33. Projection of guidance and robotic testbed tracking on ADAMUS testbed**

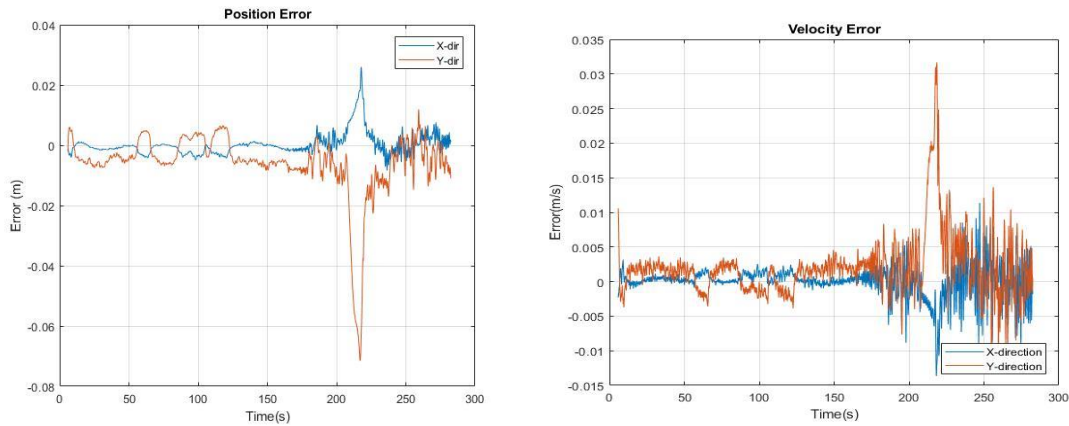


**Figure 34. ADAMUS testbed reference tracking position and velocity error**

The testbed results showed a maximum position error of 0.07 m and a maximum velocity error of 0.03 m/s. These errors may be attributed to physical errors in the testbed. The errors tend to increase towards the end of the experiment, possibly due to low fuel in the air tanks of the testbed.

## 5.0 CONCLUSIONS

This work responds to the pressing need of the Air Force to better understand and utilize the dynamics, guidance, control and navigation of satellite relative motion for close-proximity missions. The contract research objectives have been fulfilled by introducing major advances in the state-of-the-art of spacecraft relative motion dynamics, guidance, control, navigation and high-fidelity hardware-in-the-loop validation. These advances are summarized at high level in this report and have been extensively disseminated in peer reviewed conference and journal publications, as enumerated in Section 6.0.

## 6.0 REFERENCES

- 1) Sullivan J., Grimberg S., D'Amico S., "Comprehensive Survey and Assessment of Spacecraft Relative Motion Dynamics Models," *Journal of Guidance, Control, and Dynamics*, **Vol. 40**, No. 8, August 2017, pp. 1837-1859.
- 2) G. Di Mauro, M. Lawn, R. Bevilacqua, "Survey on Guidance Navigation and Control Requirements for Spacecraft Formation Flying Missions," *Journal of Guidance, Control, and Dynamics*, **Vol. 41**, No. 3, March 2018, pp. 581-602.
- 3) Koenig A.W., Guffanti T., D'Amico S., "New State Transition Matrices for Spacecraft Relative Motion in Perturbed Orbits," *Journal of Guidance, Control, and Dynamics*, **Vol. 40**, No. 7, September 2017, pp. 1749-1768.
- 4) Guffanti T., D'Amico S., Lavagna M., "Long-Term Analytical Propagation of Satellite Relative Motion in Perturbed Orbits," *27th AAS/AIAA Space Flight Mechanics Meeting*, San Antonio, Texas, February 5-9, 2017.
- 5) Guffanti T., D'Amico S., "Linear Models for Spacecraft Relative Motion Perturbed by Solar Radiation Pressure," *Journal of Guidance, Control, and Dynamics*, **Vol. 42**, No. 9, September 2019, pp. 1962-1981.
- 6) Willis M., Lovell A., D'Amico S., "Second Order Analytical Solution for Relative Motion on Arbitrarily Eccentric Orbits," *29th AAS/AIAA Space Flight Mechanics Meeting*, Ka'anapali, Maui, HI, January 13-17, 2019.
- 7) Koenig A.W., D'Amico S., "Safe Spacecraft Swarm Deployment and Acquisition in Perturbed Near-Circular Orbits Subject to Operational Constraints," *Acta Astronautica* **Vol. 153**, December 2018, pp. 297-310.
- 8) Koenig A., D'Amico S., "Robust and Safe N-Spacecraft Swarming in Perturbed Near-Circular Orbits," *Journal of Guidance, Control, and Dynamics*, **Vol. 41**, No. 8, August 2018, pp. 1643-1662.

- 9) Guffanti T., D'Amico S., "Integration Constants as State Variables for Optimal Path Planning," *European Control Conference*, Lymassol, Cyprus, June 12-15, 2018.
- 10) M. Lawn, G. Di Mauro, R. Bevilacqua, "Guidance Solutions for Spacecraft Planar Rephasing and Rendezvous Using Input Shaping," *Journal of Guidance, Control, and Dynamics*, **Vol. 41**, No. 1, January 2018, pp. 255-267.
- 11) Chernick M., D'Amico S., "New Closed-Form Solutions for Optimal Impulsive Control of Spacecraft Relative Motion," *Journal of Guidance, Control, and Dynamics*, **Vol. 41**, No. 2, February 2018, pp. 301-319.
- 12) Chernick M., D'Amico S., "Closed-Form Optimal Impulsive Control of Spacecraft Formations using Reachable Set Theory," *2018 AAS/ALAA Astrodynamics Specialist Conference*, Snowbird, UT, August 19-23, 2018.
- 13) A.W. Koenig, S. D'Amico, "Fast Algorithm for Energy-Optimal Control of Linear Systems with Time-Varying Cost," *IEEE Transactions on Automatic Control*, 2020, Submitted.
- 14) Willis M., D'Amico S., "Relative Spiral Trajectories for Low-Thrust Formation Flying," *26th International Symposium on Space Flight Dynamics (ISSFD)*, Matsuyama, Japan, June 3-9, 2017.
- 15) Willis M., D'Amico S., "Analytical Approach to Formation-Flying with Low-Thrust Relative Spiral Trajectories," *Acta Astronautica*, **Vol. 153**, December 2018, pp.175-190.
- 16) G. Di Mauro, R. Bevilacqua, et al., "Minimum-fuel Control Strategy for Spacecraft Formation Reconfiguration via Finite-time Maneuvers," *Journal of Guidance, Control and Dynamics*, **Vol. 42**, No. 4, April 2019, pp. 752-768.
- 17) G. Di Mauro, D. Spiller, R. Bevilacqua, S. D'Amico, "Spacecraft Formation Flying Reconfiguration with Extended and Impulsive Maneuvers," *Journal of the Franklin Institute*, **Vol. 356**, No. 6, April 2019, pp. 3474-3507.
- 18) G. Di Mauro, D. Spiller, R. Bevilacqua, F. Curti, "Optimal Continuous Maneuvers for Satellite Formation Reconfiguration in J2-perturbed Orbits," *ALAA SciTech Forum*, Kissimmee, FL, January 8-12, 2018.

- 19) Di Mauro G., Bevilacqua R., Spiller D., Sullivan J., D'Amico S., "Continuous Maneuvers for Spacecraft Formation-Flying Reconfiguration using Relative Orbit Elements," *Acta Astronautica*, **Vol. 153**, December 2018, pp. 311-326.
- 20) Steindorf L., D'Amico S., Scharnagl J., Kempf F., Schilling K., "Constrained Low-Thrust Satellite Formation-Flying using Relative Orbit Elements," *27th AAS/AIAA Space Flight Mechanics Meeting*, San Antonio, Texas, February 5-9, 2017.
- 21) Sullivan J., Koenig A., D'Amico S., "Improved Maneuver-Free Approach to Angles-Only Navigation for Space Rendezvous," *26th AAS/AIAA Space Flight Mechanics Meeting*, Napa, CA, February 14-18, 2016.
- 22) Sullivan J., D'Amico S., "Adaptive Filtering for Maneuver-Free Angles-Only Navigation in Eccentric Orbits," *27th AAS/AIAA Space Flight Mechanics Meeting*, San Antonio, Texas, February 5-9, 2017.
- 23) Sullivan J., D'Amico S., "Nonlinear Kalman Filtering for Improved Angles-Only Navigation Using Relative Orbital Elements," *Journal of Guidance, Control, and Dynamics*, **Vol. 40**, No. 9, September 2017, pp. 2183-2200.
- 24) Sullivan J., Lovell A., D'Amico S., "Angles-Only Navigation for Autonomous On-Orbit Space Situational Awareness Applications," *2018 AAS/AIAA Astrodynamics Specialist Conference*, Snowbird, UT, August 19-23, 2018.
- 25) Beierle C., Sullivan J., D'Amico S., "High-Fidelity Verification of Vision-Based Sensors for Inertial and Far-Range Spacecraft Navigation," *26th International Symposium on Space Flight Dynamics (ISSFD)*, Matsuyama, Japan, June 3-9, 2017.
- 26) Beierle C., Sullivan J., D'Amico S., "Design and Utilization of the Stanford Vision-Based Navigation Testbed for Spacecraft Rendezvous," *9th International Workshop on Satellite Constellations and Formation Flight (IWSCFF)*, The University of Colorado Boulder, Colorado, June 19-21, 2017.
- 27) Beierle C., D'Amico S., "Variable Magnification Optical Stimulator for Training and Validation of Spaceborne Vision-Based Navigation," *Journal of Spacecraft and Rockets*, **Vol. 56**, No. 4, July-August 2019, pp. 1060-1072.

- 28) E. Ausay, L. Bassett-Audain, L. DeWitte, B. Paz, A. Rajbhandary, G. Di Mauro, R. Bevilacqua, "Satellite Formation Flying: On-Ground Experiment On Relative Orbit Elements-Based Control," *29th AAS/AIAA Space Flight Mechanics Meeting*, Ka'anapali, Maui, HI, January 13-17, 2019.

## DISTRIBUTION LIST

DTIC/OCF	
8725 John J. Kingman Rd, Suite	
0944 Ft Belvoir, VA 22060-6218	1 cy
AFRL/RVIL	
Kirtland AFB, NM 87117-5776	1 cy
Official Record Copy	
AFRL/RVS Thomas Lovell	1 cy